

# Neural Operator-Grounded Continuous Tensor Function Representation and Its Applications

Ruoyang Su, Xi-Le Zhao, *Senior Member, IEEE*, Sheng Liu, Wei-Hao Wu, Yisi Luo, and Michael K. Ng

**Abstract**—Recently, continuous tensor functions have attracted increasing attention, because they can unifiedly represent data both on mesh grids and beyond mesh grids. However, since mode- $n$  product is essentially discrete and linear, the potential of current continuous tensor function representations is still locked. To break this bottleneck, we suggest neural operator-grounded mode- $n$  operators as a continuous and nonlinear alternative of discrete and linear mode- $n$  product. Instead of mapping the discrete core tensor to the discrete target tensor, proposed mode- $n$  operator directly maps the continuous core tensor function to the continuous target tensor function, which provides a genuine continuous representation of real-world data and can ameliorate discretization artifacts. Empowering with continuous and nonlinear mode- $n$  operators, we propose a neural operator-grounded continuous tensor function representation (abbreviated as NO-CTR), which can more faithfully represent complex real-world data compared with classic discrete tensor representations and continuous tensor function representations. Theoretically, we also prove that any continuous tensor function can be approximated by NO-CTR. To examine the capability of NO-CTR, we suggest an NO-CTR-based multi-dimensional data completion model. Extensive experiments across various data on regular mesh grids (multi-spectral images and color videos), on mesh grids with different resolutions (Sentinel-2 images) and beyond mesh grids (point clouds) demonstrate the superiority of NO-CTR.

**Index Terms**—Continuous tensor function, tensor decomposition, neural operator, multi-dimensional data completion

## I. INTRODUCTION

**M**ULTI-DIMENSIONAL data [1]–[4] is the foundation of modern fields, and is widely used in various application scenarios, including remote sensing imaging [5], [6], object detection [7]–[9], and signal processing [10]–[12]. Effectively representing and capturing the intrinsic structure of these multi-dimensional data is crucial for tasks such as classification [13], [14], compression [15], [16], and recovery [17]–[20]. Simply flattening or vectorizing these multi-dimensional data matrices [21]–[23] often fails to maintain the high-order interactions, resulting in poor performance and interpretability. Therefore, developing effective methods to represent and process multi-dimensional data still remains a fundamental challenge.

As natural extensions of vectors and matrices to higher dimensions, tensors have become fundamental and common

(Corresponding author: Xi-Le Zhao)

Ruoyang Su, Xi-Le Zhao, Sheng Liu and Wei-Hao Wu are with the School of Mathematical Sciences, University of Electronic Science and Technology of China, Chengdu 611731, China (e-mail: 202511110508@std.uestc.edu.cn; xilzhao122003@163.com; liusheng16@163.com; weihao99@163.com).

Yisi Luo is with the School of Mathematics and Statistics, Xi’an Jiaotong University, Xi’an 710049, China (e-mail: yisiluo1221@foxmail.com).

Michael K. Ng is with the Department of Mathematics, Hong Kong Baptist University, Hong Kong, China (e-mail: michael-ng@hkbu.edu.hk).

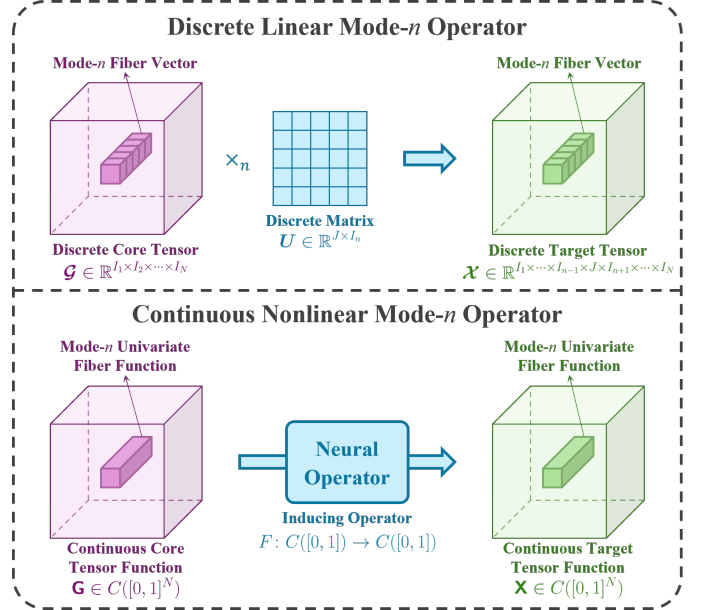


Fig. 1. Discrete and linear mode- $n$  operator and proposed continuous and nonlinear mode- $n$  operator. The basic unit performed upon by discrete and linear mode- $n$  operator is the mode- $n$  fiber vectors of the discrete core tensor  $\mathcal{G}$ , which are then mapped to the mode- $n$  fiber vectors of the discrete target tensor  $\mathcal{X}$ . The basic unit performed upon by continuous and nonlinear mode- $n$  operator is the mode- $n$  univariate fiber functions of the continuous core tensor function  $\mathbf{G}$ , which are then mapped to the mode- $n$  univariate fiber functions of the continuous target tensor function  $\mathbf{X}$ .

structures for representing multi-dimensional data. Traditional tensor methods mainly focus on low-rank decompositions. The CANDECOMP/PARAFAC (CP) decomposition [24], [25] aims to decompose a tensor into the sum of rank-one components. The Tucker decomposition [26] focuses on decomposing a tensor into a core tensor multiplied by matrices along each mode. The tensor singular value decomposition (t-SVD) [27]–[29] is designed to decompose a third-order tensor into the t-product of an f-diagonal tensor and two orthogonal tensors. The tensor train (TT) decomposition [30] involves decomposing an  $N$ th-order tensor into a sequence of a matrix,  $N - 2$  third-order tensors, and another matrix. The tensor ring (TR) decomposition [31] is characterized by decomposing an  $N$ th-order tensor into  $N$  third-order tensors multiplied in a circular manner.

The emergence of continuous tensor functions has revolutionized multi-dimensional data representation. By mapping the coordinates to corresponding data values, continuous tensor functions eliminate the dependency on fixed mesh grids, and seamlessly unify data on mesh grids and beyond mesh

grids into a single flexible framework, providing a more flexible representation of multi-dimensional data. Borrowing the wisdom of traditional tensor decompositions, researchers have developed a series of continuous tensor function representations. Imaizumi et al. [32] proposed the smoothed Tucker decomposition (STD), which approximates an observed tensor by a small number of basis functions, and decomposes them through Tucker decomposition. Fang et al. [33] proposed functional Bayesian Tucker decomposition (FunBaT). They treat the continuous-indexed data as the interaction between the Tucker core and a group of latent functions, and use Gaussian processes as functional priors to model the latent functions. Furthermore, Luo et al. [34] proposed a low-rank tensor function representation (LRTFR) parameterized by multi-layer perceptrons, which can continuously represent data beyond meshgrid with powerful representation abilities. Despite this breakthrough, existing continuous tensor function representations are constrained by a fundamental limitation: the mappings (mode- $n$  product) from discrete core tensors to discrete target tensors are essentially discrete and linear, which renders them inadequate for capturing the complex structure of real-world data, leaving the potential of continuous tensor functions largely locked.

To break this bottleneck, in this paper, we suggest a continuous and nonlinear alternative of mode- $n$  product, i.e. continuous and nonlinear mode- $n$  operators. To achieve this goal, we introduce neural operators [35]–[37] into the field of continuous tensor function representations for the first time, to genuinely capture the complex structure of real-world data. Concretely, we leverage a neural operator to directly map the mode- $n$  univariate functions of the continuous core tensor function to those functions of the continuous target tensor function. Then we propose a neural operator-grounded continuous tensor function representation (NO-CTR), to faithfully represent complex real-world data as a continuous core tensor function composite with a series of continuous and nonlinear mode- $n$  operators. Figure 1 compares previous discrete and linear mode- $n$  operators and proposed continuous and nonlinear mode- $n$  operators. Benefit from the powerful capability of continuous and nonlinear mode- $n$  operators to capture nonlinear relations, proposed NO-CTR can represent complex real-world data more faithfully. NO-CTR not only unlocks the potential of continuous tensor functions, but also bridges the gap between neural operators and tensor representations.

The main contributions of this paper are as follows:

- (1) To break the limitation of discrete and linear mode- $n$  product, we suggest neural operator-grounded mode- $n$  operators as a continuous and nonlinear alternative, which provides a genuine continuous representation of real-world data and can ameliorate discretization artifacts.
- (2) Empowering with continuous and nonlinear mode- $n$  operators, we propose a neural operator-grounded continuous tensor function representation (NO-CTR), which can faithfully represent complex real-world data.
- (3) Theoretically, we prove that any continuous tensor function can be approximated by NO-CTR. Besides, to examine the capability of NO-CTR, we suggest an NO-CTR-based multi-dimensional data completion model.

- (4) Extensive experiments across various data on regular mesh grids (multi-spectral images and color videos), on mesh grids with different resolutions (Sentinel-2 images) and beyond mesh grids (point clouds) demonstrate the superiority of NO-CTR.

## II. RELATED WORK

### A. Continuous Tensor Function Representations

One of the most popular continuous tensor function representations is implicit neural representation (INR), whose aim is to use a deep neural network to learn the continuous tensor function of the multi-dimensional data with respect to the coordinates. It was originally used for 3D shape representation, such as [38], [39]. After that, it was also widely used for representing various multi-dimensional data. Sitzmann et al. [40] proposed to leverage periodic activation functions for implicit neural representations and demonstrated that these networks (called SIRENs) are ideally suited for representing complex natural signals and their derivatives. Tancik et al. [41] suggested an approach for selecting problem-specific Fourier features that greatly improves the performance of multi-layer perceptrons (MLPs) for low-dimensional regression tasks relevant to the computer vision and graphics communities. Saragadam et al. [42] developed a new, highly accurate and robust INR: wavelet implicit neural representation (WIRE), a new INR based on a complex Gabor wavelet activation function. Shi et al. [43] proposed a Fourier reparameterization method which learns coefficient matrix of fixed Fourier bases to compose the weights of multi-layer perceptron. Recently, numerous researchers have extensive much work [44]–[49] in this area. INR provides a novel representation for multi-dimensional data, but it does not take into account the intrinsic structure and the interactions between factors of multi-dimensional data.

### B. Neural Operators

Recently, neural operators have received extensive attention in scientific computing. In mathematics, a neural operator is a mapping from one function to another [50], [51], with nonlinear structures and powerful capabilities. They have demonstrated great potential in solving partial differential equations usually by learning a mapping from the parameter function to the solution function [52]. Anandkumar et al. [35] formulated approximation of the infinite-dimensional mapping by composing nonlinear activation functions and a class of integral operators, where kernel integration is computed by message passing on graph networks. Lu et al. [36] proposed a general deep learning framework, the deep operator network (DeepONet), to learn diverse continuous and nonlinear operators. Li et al. [37] formulated a new neural operator by parameterizing the integral kernel directly in Fourier space, allowing for an expressive and efficient architecture. In summary, neural operators are powerful tools usually with nonlinear structures, which can flexibly map from one function to another.

### III. NOTATIONS AND PRELIMINARIES

Throughout this paper, scalars, vectors, matrices, and (discrete) tensors are denoted by  $x$ ,  $\mathbf{x}$ ,  $\mathbf{X}$ , and  $\mathcal{X}$ , respectively. And  $\mathcal{X}(i_1, i_2, \dots, i_N)$  denotes the  $(i_1, i_2, \dots, i_N)$ th element of an  $N$ th-order discrete tensor  $\mathcal{X} \in \mathbb{R}^{I_1 \times I_2 \times \dots \times I_N}$ .

An  $N$ th-order continuous tensor function<sup>1</sup>, denoted by  $\mathbf{X}$ , is an  $N$ -variable continuous function with a dense and complete domain, whose input is a coordinate with  $N$  dimensions, and whose output is the corresponding value in the target data. Without loss of generality, in this paper, we normalize the coordinates to  $[0, 1]$ , so  $\mathbf{X} \in C([0, 1]^N)$ .

Fibers are the higher-order analogue of matrix rows and columns. A fiber is defined by fixing every index but one [54]. For discrete tensor  $\mathcal{X} \in \mathbb{R}^{I_1 \times I_2 \times \dots \times I_N}$ , the mode- $n$  fiber vectors are denoted by

$$\mathcal{X}(i_1, i_2, \dots, i_{n-1}, :, i_{n+1}, \dots, i_N) \in \mathbb{R}^{I_n}.$$

Similarly, for continuous tensor function  $\mathbf{X} \in C([0, 1]^N)$ , the mode- $n$  univariate fiber functions are denoted by

$$\mathbf{X}(y_1, y_2, \dots, y_{n-1}, \cdot, y_{n+1}, \dots, y_N) \in C([0, 1]).$$

*Definition 1 (Mode- $n$  Unfolding [54]):* Given a discrete tensor  $\mathcal{X} \in \mathbb{R}^{I_1 \times I_2 \times \dots \times I_N}$ , the mode- $n$  unfolding, denoted by  $\mathbf{X}_{(n)}$ , arranges mode- $n$  fiber vectors to be the columns of the resulting matrix, which is defined as follows:

$$\mathbf{X}_{(n)}(i_n, j) = \mathcal{X}(i_1, i_2, \dots, i_n, \dots, i_N),$$

where  $j = 1 + \sum_{\substack{k=1 \\ k \neq n}}^N (i_k - 1) \prod_{\substack{m=1 \\ m \neq n}}^{k-1} I_m$ , and  $n = 1, 2, \dots, N$ . The

inverse operation of mode- $n$  unfolding is denoted as  $\text{fold}_n$ , i.e.  $\mathcal{X} = \text{fold}_n(\mathbf{X}_{(n)})$ .

### IV. REVISIT OF MODE- $n$ PRODUCT

Previous tensor representations typically represent a tensor as a set of factors. The operations or connections between factors largely determine the representation capability. In this section, we will revisit them from a new perspective—the perspective of operators.

Mode- $n$  product is widely used in tensor representations, which is defined as follows:

*Definition 2 (Mode- $n$  Product [54]):* Given an  $N$ th-order discrete tensor  $\mathcal{G} \in \mathbb{R}^{I_1 \times I_2 \times \dots \times I_N}$  and a matrix  $\mathbf{U} \in \mathbb{R}^{J \times I_n}$ , the mode- $n$  product  $\mathcal{G} \times_n \mathbf{U} \in \mathbb{R}^{I_1 \times \dots \times I_{n-1} \times J \times I_{n+1} \times \dots \times I_N}$  is defined as

$$\begin{aligned} & \mathcal{G} \times_n \mathbf{U}(i_1, i_2, \dots, i_{n-1}, j, i_{n+1}, \dots, i_N) \\ &= \sum_{i_n=1}^{I_n} \mathcal{G}(i_1, i_2, \dots, i_{n-1}, i_n, i_{n+1}, \dots, i_N) \mathbf{U}(j, i_n), \end{aligned}$$

which can also be equivalently expressed as

$$\mathcal{G} \times_n \mathbf{U} = \text{fold}_n(\mathbf{U} \mathbf{G}_{(n)}),$$

where  $n = 1, 2, \dots, N$ .

<sup>1</sup>There are other names of this concept in previous literature, such as continuous-indexed tensor [33], functional tensor [53], tensor function [34].

To better understand the role of mode- $n$  product, we reinterpret it from the perspective of operators:

*Definition 3 (Discrete and Linear Mode- $n$  Operator):* Given an  $N$ th-order discrete tensor  $\mathcal{G} \in \mathbb{R}^{I_1 \times I_2 \times \dots \times I_N}$  and a matrix  $\mathbf{U} \in \mathbb{R}^{J \times I_n}$ , the discrete and linear mode- $n$  operator

$$\mathcal{U}^{[n]}: \mathbb{R}^{I_1 \times \dots \times I_n \times \dots \times I_N} \rightarrow \mathbb{R}^{I_1 \times \dots \times I_{n-1} \times J \times I_{n+1} \times \dots \times I_N}$$

induced by  $\mathbf{U}$  is defined as

$$\begin{aligned} & \mathcal{U}^{[n]}(\mathcal{G})(i_1, i_2, \dots, i_{n-1}, j, i_{n+1}, \dots, i_N) \\ &= (\mathbf{U} \mathcal{G}(i_1, i_2, \dots, i_{n-1}, :, i_{n+1}, \dots, i_N))(j), \end{aligned} \quad (1)$$

where  $n = 1, 2, \dots, N$ .

Combined with Definition 2, it is easy to identify that discrete and linear mode- $n$  operators are equivalent to mode- $n$  product, i.e.

$$\mathcal{U}^{[n]}(\mathcal{G}) = \mathcal{G} \times_n \mathbf{U}.$$

As shown in Figure 1, the basic unit performed upon by discrete and linear mode- $n$  operator  $\mathcal{U}^{[n]}$  is the mode- $n$  fiber vectors

$$\mathcal{G}(i_1, i_2, \dots, i_{n-1}, :, i_{n+1}, \dots, i_N) \in \mathbb{R}^{I_n}$$

of the discrete tensor  $\mathcal{G}$ , which are then mapped to the mode- $n$  fiber vectors

$$\mathcal{U}^{[n]}(\mathcal{G})(i_1, i_2, \dots, i_{n-1}, :, i_{n+1}, \dots, i_N) \in \mathbb{R}^J$$

of the discrete target tensor  $\mathcal{U}^{[n]}(\mathcal{G})$ . Therefore, in mode- $n$  product, the mapping from  $\mathcal{G}$  to  $\mathcal{U}^{[n]}(\mathcal{G})$  is inherently discrete and linear.

From the perspective of operators, we review the previous representations Tucker decomposition [26] and LRTFR [34] in this perspective. They both represent the discrete target tensor as a discrete core tensor composite with a set of discrete and linear mode- $n$  operators. In mathematics, both of them can be reformulated as

$$\mathcal{X} = \mathcal{U}^{[N]} \circ \dots \circ \mathcal{U}^{[2]} \circ \mathcal{U}^{[1]}(\mathcal{G}), \quad (2)$$

where  $\mathcal{G}$  is the discrete core tensor, and  $\mathcal{U}^{[n]}$  is the discrete and linear mode- $n$  operator induced by factor matrix  $\mathbf{U}_n$  ( $n = 1, 2, \dots, N$ ). In Tucker decomposition [26],  $\{\mathbf{U}_n\}_{n=1}^N$  are ordinary matrices, while in LRTFR [34],  $\{\mathbf{U}_n\}_{n=1}^N$  are matrices sampled from functions implemented by implicit neural representations. Although the core tensor or factor matrices can be generated by neural networks, the mapping from discrete core tensor  $\mathcal{G}$  to discrete target tensor  $\mathcal{X}$  is essentially linear, which limits the capabilities of these representations. Besides, the real-world data are usually complex and contain generous nonlinear relations, which are also difficult to precisely capture merely through linear mappings.

### V. NEURAL OPERATOR-GROUNDED CONTINUOUS TENSOR FUNCTION REPRESENTATION

In this section, we will propose continuous and nonlinear mode- $n$  operators. Empowering with this, we will propose a neural operator-grounded continuous tensor function representation (NO-CTR), and will prove that any continuous tensor function can be approximated by NO-CTR. Lastly, we will suggest an NO-CTR-based multi-dimensional data completion model.

### A. Continuous and Nonlinear Mode- $n$ Operators

To break the above limitations of discrete and linear mode- $n$  operators, in this subsection, we will propose continuous and nonlinear mode- $n$  operators.

In Section IV, we revisited mode- $n$  product from the perspective of operators. In this perspective, the basic unit performed upon by discrete and linear mode- $n$  operator is the mode- $n$  fiber vectors. This perspective inspires us to define new interactions for continuous tensor functions. Specifically, proposed continuous and nonlinear mode- $n$  operators directly perform on the mode- $n$  univariate fiber functions of a continuous tensor function, preserving this key property of discrete and linear mode- $n$  operators. Below we provide a definition of continuous and nonlinear mode- $n$  operators.

**Definition 4 (Continuous and Nonlinear Mode- $n$  Operator):** Given an  $N$ th-order continuous tensor function  $\mathbf{G} \in C([0, 1]^N)$  and a continuous operator  $F: C([0, 1]) \rightarrow C([0, 1])$ , the continuous and nonlinear mode- $n$  operator

$$\mathcal{F}^{(n)}: C([0, 1]^N) \rightarrow C([0, 1]^N)$$

induced by  $F$  is defined as

$$\begin{aligned} & \mathcal{F}^{(n)}(\mathbf{G})(y_1, y_2, \dots, y_N) \\ &= F(\mathbf{G}(y_1, y_2, \dots, y_{n-1}, \cdot, y_{n+1}, \dots, y_N))(y_n), \end{aligned} \quad (3)$$

where  $n = 1, 2, \dots, N$ . To avoid confusion, we refer to  $F$  as the inducing operator.

In Equation (3), we start from a continuous tensor function  $\mathbf{G}$  instead of a discrete tensor  $\mathcal{G}$ . As shown in Figure 1, the basic unit performed upon by continuous and nonlinear mode- $n$  operator  $\mathcal{F}^{(n)}$  is the mode- $n$  univariate fiber functions

$$\mathbf{G}(y_1, y_2, \dots, y_{n-1}, \cdot, y_{n+1}, \dots, y_N) \in C([0, 1])$$

of the continuous tensor function  $\mathbf{G}$ , which are then mapped to the mode- $n$  univariate fiber functions

$$F(\mathbf{G}(y_1, y_2, \dots, y_{n-1}, \cdot, y_{n+1}, \dots, y_N)) \in C([0, 1])$$

of the continuous target tensor function  $\mathcal{F}^{(n)}(\mathbf{G})$ . Besides, the inducing operator  $F$  is usually nonlinear, so the continuous and nonlinear mode- $n$  operator is a nonlinear mapping from  $\mathbf{G}$  to  $\mathcal{F}^{(n)}(\mathbf{G})$ .

Finally, we use experimental results to further display the advantages of continuous and nonlinear operations. Figure 2 shows the visual and quantitative recovery results with discrete and linear mode- $n$  operators (LRTFR [34]), continuous and nonlinear mode- $n$  operators (proposed NO-CTR) when the sampling rates are 10%. In terms of quantitative results, proposed NO-CTR outperforms LRTFR on various multi-dimensional data. In terms of visual results, proposed NO-CTR is capable of more accurately recovering details, such as the stripes on clothes and the eyes of frogs. This reveals the superiority of proposed continuous and nonlinear mode- $n$  operators.

### B. Continuous Tensor Function Representation

Empowering with continuous and nonlinear mode- $n$  operators, in this subsection, we will propose a neural operator-grounded continuous tensor function representation (NO-CTR). Here we present a mathematical definition.

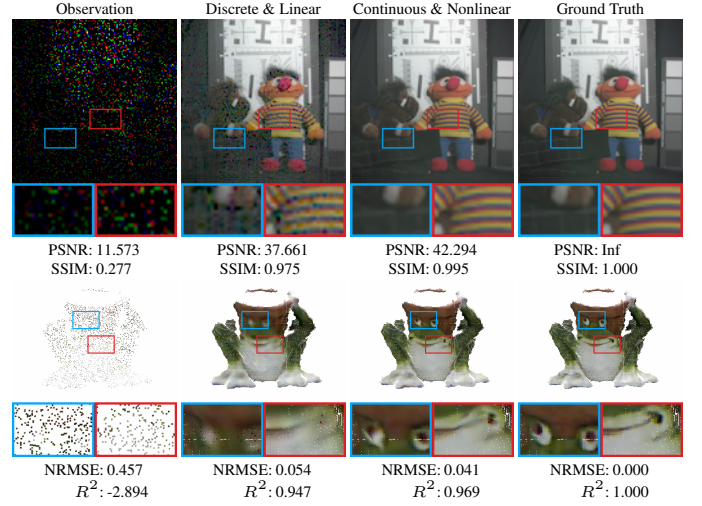


Fig. 2. Visual and quantitative recovery results with discrete and linear mode- $n$  operators (LRTFR [34]), continuous and nonlinear mode- $n$  operators (proposed NO-CTR) on the MSI Toy (top) and point cloud Frog (bottom) when the sampling rates are 10%.

**Definition 5 (NO-CTR):** For an  $N$ th-order continuous tensor function  $\mathbf{X} \in C([0, 1]^N)$ , the neural operator-grounded continuous tensor function representation (abbreviated as NO-CTR) of  $\mathbf{X}$  can be formulated as

$$\mathbf{X} = \mathcal{F}_N^{(N)} \circ \dots \circ \mathcal{F}_2^{(2)} \circ \mathcal{F}_1^{(1)}(\mathbf{G}), \quad (4)$$

where  $\mathbf{G} \in C([0, 1]^N)$  is the continuous core tensor function, and  $\mathcal{F}_n^{(n)}$  is the continuous and nonlinear mode- $n$  operator induced by  $F_n$  ( $n = 1, 2, \dots, N$ ).

In Equation (2), the previous representations Tucker decomposition [26] and LRTFR [34] represent the discrete target tensor  $\mathcal{X}$  as a discrete core tensor  $\mathcal{G}$  composite with a set of discrete and linear mode- $n$  operators  $\{\mathcal{U}^{[n]}\}_{n=1}^N$ . Similarly, in Equation (4), proposed NO-CTR represents complex real-world data  $\mathbf{X}$  as a continuous core tensor function  $\mathbf{G}$  composite with a series of continuous and nonlinear mode- $n$  operators  $\{\mathcal{F}^{(n)}\}_{n=1}^N$ . Owing to the powerful capability of the continuous mode- $n$  operation to capture nonlinear relations, NO-CTR can represent complex real-world data more faithfully.

### C. Implementations

In Equation (4), the continuous core tensor function  $\mathbf{G}$  and continuous and nonlinear mode- $n$  operators  $\{\mathcal{F}^{(n)}\}_{n=1}^N$  are the key components of NO-CTR. In this subsection, we discuss the concrete implementations.

1) *Continuous Core Tensor Function:* The continuous core tensor function  $\mathbf{G} \in C([0, 1]^N)$  is essentially a multivariate continuous function defined on  $[0, 1]^N$ . In practice, neural networks are ideally suited for representing such continuous functions, and the choice of neural networks is highly diverse. In this paper, we choose the popular implicit neural representation SIREN [40] to implement this continuous core tensor function  $\mathbf{G}$ , which takes a coordinate  $\mathbf{y} \in [0, 1]^N$  as input and outputs its corresponding value  $\mathbf{G}(\mathbf{y}) \in \mathbb{R}$ . We will also discuss other implementations of the continuous core tensor function in Section VII-C.

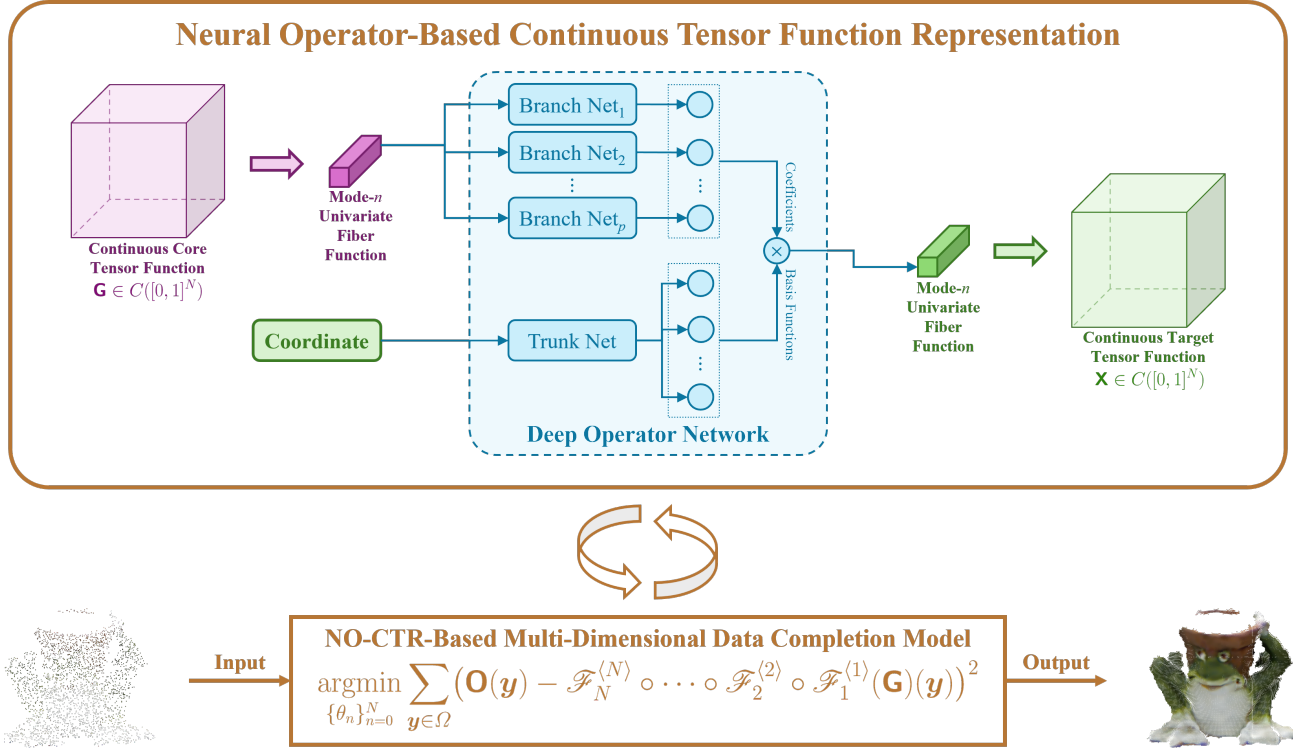


Fig. 3. Flow chart of NO-CTR and the corresponding multi-dimensional data completion model. We first cleverly leverage neural operators to suggest continuous and nonlinear mode- $n$  operators. Specifically, the basic unit performed upon by continuous and nonlinear mode- $n$  operator is the mode- $n$  univariate fiber functions of the continuous core tensor function  $\mathbf{G}$ , which are then mapped to the mode- $n$  univariate fiber functions of the continuous target tensor function  $\mathbf{X}$ . Empowering with continuous and nonlinear mode- $n$  operators, we propose a neural operator-grounded continuous tensor function representation (NO-CTR), which can faithfully represent continuous target tensor function  $\mathbf{X}$  as a continuous core tensor function  $\mathbf{G}$  and a series of continuous and nonlinear mode- $n$  operators  $\{\mathcal{F}^{(n)}\}_{n=1}^N$ . To examine the capability of NO-CTR, we suggest an NO-CTR-based multi-dimensional data completion model.

2) *Continuous and Nonlinear Mode- $n$  Operators*: In mathematics, any function operator can be utilized to implement the continuous and nonlinear mode- $n$  operator. In this paper, we cleverly leverage an emerging and powerful tool: neural operators, which provide a correct and efficient choice for us. Neural operators play a significant role in scientific computing [35]–[37]. Essentially, a neural operator is a mapping from one function to another [50], [51]. This enables us to directly treat a neural operator as the inducing operator, marking the first application of neural operators in the field of tensor representations.

Among the diverse neural operators, we select the deep operator networks (DeepONet) [34] to implement continuous and nonlinear mode- $n$  operators, and will discuss other architectures of neural operators in Section VII-B. DeepONet is composed of the trunk network and branch networks. Specifically, for an inducing operator  $F_n: C([0, 1]) \rightarrow C([0, 1])$ ,

$$F_n(v)(y) = \sum_{p=1}^{P_n} b_p^{(n)}(v(z_1), v(z_2), \dots, v(z_{m_n})) t_p^{(n)}(y),$$

where  $v \in C([0, 1])$  is the input univariate function,  $y \in [0, 1]$  is a coordinate.  $\mathbf{t}^{(n)}$  is a vector-valued function called trunk network, and  $\{t_p^{(n)}\}_{p=1}^{P_n}$  are  $P$  components of  $\mathbf{t}$ , which can be physically interpreted as the basis functions of the output space.  $\{b_p^{(n)}\}_{p=1}^{P_n}$  are scalar-valued functions called branch networks, which encode the discrete sampling values of input

function  $v$  at fixed sensor points  $\{z_i\}_{i=1}^{m_n}$  (called sensors), providing the coefficients required for the linear combination.

#### D. Universal Approximation Theorem

To theoretically illustrate the rationality of the above implementations, we propose and prove the density of the NO-CTR, which indicates any continuous tensor function can be approximated by NO-CTR, and can be regarded as a universal approximation theorem.

*Theorem 1*: For any continuous tensor function  $\mathbf{X} \in C([0, 1]^N)$ ,  $\forall \varepsilon > 0$ , there is a fully connected neural network

$$\mathbf{G}: [0, 1]^N \rightarrow \mathbb{R}$$

and  $N$  DeepONets [36]

$$F_n: C([0, 1]) \rightarrow C([0, 1]), \quad (n = 1, 2, \dots, N)$$

such that

$$\|\mathbf{X} - \mathcal{F}_N^{(N)} \circ \dots \circ \mathcal{F}_2^{(2)} \circ \mathcal{F}_1^{(1)}(\mathbf{G})\| < \varepsilon,$$

where  $\mathcal{F}_n$  is the continuous and nonlinear mode- $n$  operator induced by  $F_n$ .

The proof can be found in the appendix.

### E. Multi-Dimensional Data Completion Model

To examine the capability of the NO-CTR, we suggest an NO-CTR-based multi-dimensional data completion model, which aims to estimate the missing elements from an incomplete observation.

In mathematics, this model can be formulated as

$$\operatorname{argmin}_{\{\theta_n\}_{n=0}^N, \mathbf{y} \in \Omega} (\mathbf{O}(\mathbf{y}) - \mathcal{F}_N^{(N)} \circ \dots \circ \mathcal{F}_2^{(2)} \circ \mathcal{F}_1^{(1)}(\mathbf{G})(\mathbf{y}))^2, \quad (5)$$

where  $\mathbf{O} \in C([0, 1]^N)$  is the continuous tensor function of the observation,  $\mathbf{y}$  is a coordinate,  $\Omega \subseteq [0, 1]^N$  is a set composed of the coordinates of all observed elements,  $\mathbf{G} \in C([0, 1]^N)$  is the continuous core tensor function,  $\mathcal{F}_n$  is the continuous and nonlinear mode- $n$  operator induced by  $F_n$ ,  $\theta_0$  denotes the parameters of the continuous core tensor function  $\mathbf{G}$ , and  $\theta_n$  denotes the parameters of the inducing operator  $F_n$  ( $n = 1, 2, \dots, N$ ).

## VI. EXPERIMENTS

To comprehensively evaluate the performance of the NO-CTR, we conduct extensive experiments across various data on regular mesh grids (multi-spectral images and color videos), on mesh grids with different resolutions (Sentinel-2 images) and beyond mesh grids (point clouds). In these experiments, observations are generated by randomly sampling the original ground truth at four different rates: 5%, 10%, 15%, and 20%. All methods use only one observation as training data in each experiment.

For data on mesh grids, the competing methods include both traditional tensor methods (TR-ALS [55]) and continuous representation methods (SIREN [40], MFN [44], FR-INR [43] and LRTFR [34]); for data beyond mesh grids, since traditional tensor methods cannot handle them, the competing methods only include continuous representation methods (SIREN [40], MFN [44], FR-INR [43] and LRTFR [34]). In terms of implementation, TR-ALS [55] is coded in MATLAB, and the other methods are implemented based on the PyTorch library within the Anaconda environment.

The hyper-parameter configurations for all baseline methods strictly follow the settings reported in their original publications or the official source code provided by the authors. For proposed NO-CTR, the hyper-parameters are adjusted based on the relevant literature [34], [40] combined with extensive empirical tuning. Besides, considering the structure of multi-dimensional data and the limitation of computing power, in the experiments of this paper, we set all the continuous and nonlinear mode- $n$  operators along the spatial modes as identity operators. During the training loop, quantitative evaluations are conducted every 100 iterations by comparing the recovered output with the ground truth, and the checkpoint that yields the optimal performance is selected as the final result.

For an objective and quantitative comparison, four widely adopted metrics are employed to evaluate the reconstruction quality: peak signal-to-noise ratio (PSNR), structural similarity (SSIM) [56], normalized root mean square error (NRMSE), and coefficient of determination ( $R^2$ ) as quality metrics. Generally, superior reconstruction quality is indicated by higher

PSNR, SSIM, and  $R^2$  values, as well as a lower NRMSE value.

### A. Multi-Spectral Images

First, we conduct experiments on traditional and classic multi-dimensional data on regular mesh grids: multi-spectral images (MSI). We use a database [57] that spans a wide variety of real world materials. Each multi-dimensional image is resized to  $128 \times 128$  pixels with 31 bands.

Table I lists the quantitative recovery results of MSI completion. Proposed NO-CTR demonstrates superior performance across all experimental settings: it achieves the highest PSNR and SSIM values among all competing methods for all MSIs and all sampling rates. This advantage is consistent at low sampling rates, and becomes more pronounced as the sampling rates increase. Figure 4 shows the visual recovery results of MSI completion when the sampling rates are 10%. Proposed NO-CTR demonstrates remarkable performance in recovering fine details and textures. Compared with other methods, the results recovered by proposed NO-CTR are much closer to the ground truth.

### B. Color Videos

Then, we conduct experiments on higher-order multi-dimensional data on regular mesh grids: color videos, which consist of a temporally ordered sequence of frames. Each color video is resized to  $144 \times 176$  pixels with three color channels (RGB) and consists of 30 consecutive frames.

Table II lists the quantitative recovery results of color video completion. Proposed NO-CTR consistently outperforms all competing methods across all color videos and all sampling rates, achieving the highest PSNR and SSIM values in every experimental setting. This superiority is evident at high sampling rates, and it maintains this lead at low sampling rates. Figure 5 shows the visual recovery results of color video completion when the sampling rates are 10%. Proposed NO-CTR effectively restores the visual details of dynamic scenes. In terms of these color videos, proposed NO-CTR outperforms competing methods by recovering clearer textures and sharper edges, thus better retaining the visual information of the color videos.

### C. Sentinel-2 Images

Next, we conduct experiments on multi-dimensional data on mesh grids with different spatial resolutions: Sentinel-2 images. Sentinel-2 is an European mission that utilizes wide-swath, high-resolution, multi-spectral imaging. It is equipped with an optical instrument payload that samples 13 spectral bands, including: four bands at 10 m, six bands at 20 m, and three bands at 60 m spatial resolution. The corresponding images are cropped to  $300 \times 300$  pixels,  $150 \times 150$  pixels, and  $50 \times 50$  pixels, respectively.

Table III lists the quantitative recovery results of Sentinel-2 image completion. Proposed NO-CTR method exhibits outstanding performance across all three datasets and all evaluated sampling rates, outperforming competing methods in nearly

TABLE I  
QUANTITATIVE RECOVERY RESULTS OF MSI COMPLETION

| Sampling Rate  |             | 5%            |              |              | 10%           |              |              | 15%           |              |              | 20%           |              |              |
|--|-------------|---------------|--------------|--------------|---------------|--------------|--------------|---------------|--------------|--------------|---------------|--------------|--------------|
| MSI  | Method      | PSNR          | SSIM         | NRMSE        |
|   | Observation | 15.532        | 0.045        | 0.274        | 15.769        | 0.078        | 0.266        | 16.023        | 0.112        | 0.259        | 16.277        | 0.148        | 0.251        |
|  | TR-ALS      | 26.918        | 0.672        | 0.074        | 30.129        | 0.841        | 0.051        | 31.514        | 0.879        | 0.043        | 31.977        | 0.890        | 0.041        |
|  | SIREN       | 29.737        | 0.842        | 0.053        | 34.377        | 0.946        | 0.031        | 37.860        | 0.982        | 0.021        | 41.742        | 0.992        | 0.013        |
|  | MFN         | 28.507        | 0.806        | 0.061        | 31.843        | 0.907        | 0.042        | 36.741        | 0.975        | 0.024        | 40.022        | 0.989        | 0.016        |
|  | FR-INR      | 32.099        | <u>0.918</u> | <u>0.041</u> | <u>37.273</u> | <u>0.977</u> | <u>0.022</u> | <u>41.133</u> | <u>0.991</u> | <u>0.014</u> | <u>43.701</u> | <u>0.995</u> | <u>0.011</u> |
|  | LRTFR       | 30.631        | 0.859        | 0.048        | 34.300        | 0.946        | 0.032        | 37.817        | 0.977        | 0.021        | 40.461        | 0.988        | 0.016        |
|  | NO-CTR      | <b>33.906</b> | <b>0.943</b> | <b>0.033</b> | <b>39.188</b> | <b>0.985</b> | <b>0.018</b> | <b>42.793</b> | <b>0.994</b> | <b>0.012</b> | <b>45.579</b> | <b>0.997</b> | <b>0.009</b> |
|   | Observation | 16.269        | 0.372        | 0.168        | 16.497        | 0.403        | 0.163        | 16.744        | 0.436        | 0.159        | 17.010        | 0.468        | 0.154        |
|  | TR-ALS      | 27.399        | 0.729        | 0.047        | 31.348        | 0.873        | 0.030        | 34.373        | 0.921        | 0.021        | 35.974        | 0.933        | 0.017        |
|  | SIREN       | 33.706        | 0.925        | 0.023        | 38.681        | 0.977        | 0.013        | 41.702        | 0.989        | 0.009        | 46.041        | <u>0.995</u> | 0.005        |
|  | MFN         | 29.564        | 0.823        | 0.036        | 35.092        | 0.943        | 0.019        | 39.800        | 0.977        | 0.011        | 43.464        | 0.989        | 0.007        |
|  | FR-INR      | 34.713        | <u>0.941</u> | <u>0.020</u> | <u>39.783</u> | <u>0.981</u> | <u>0.011</u> | <u>43.309</u> | <u>0.991</u> | <u>0.007</u> | <u>46.686</u> | 0.994        | <u>0.005</u> |
|  | LRTFR       | 33.619        | 0.930        | 0.023        | 36.879        | 0.965        | 0.016        | 40.100        | 0.984        | 0.011        | 43.249        | 0.991        | 0.008        |
|  | NO-CTR      | <b>37.121</b> | <b>0.981</b> | <b>0.015</b> | <b>42.591</b> | <b>0.994</b> | <b>0.008</b> | <b>46.456</b> | <b>0.997</b> | <b>0.005</b> | <b>49.717</b> | <b>0.999</b> | <b>0.004</b> |
|   | Observation | 16.574        | 0.105        | 0.258        | 16.810        | 0.141        | 0.251        | 17.059        | 0.177        | 0.244        | 17.328        | 0.214        | 0.237        |
|  | TR-ALS      | 29.634        | 0.789        | 0.057        | 33.219        | 0.892        | 0.038        | 35.558        | 0.928        | 0.029        | 36.321        | 0.938        | 0.027        |
|  | SIREN       | 34.747        | 0.918        | 0.032        | 39.731        | 0.973        | 0.018        | 43.023        | 0.986        | 0.012        | 46.164        | 0.994        | 0.009        |
|  | MFN         | 32.563        | 0.863        | 0.041        | 37.103        | 0.943        | 0.024        | 41.731        | 0.980        | 0.014        | 44.520        | 0.990        | 0.010        |
|  | FR-INR      | 35.374        | <u>0.934</u> | <u>0.030</u> | <u>40.407</u> | <u>0.977</u> | <u>0.017</u> | <u>43.850</u> | <u>0.989</u> | <u>0.011</u> | <u>46.953</u> | <u>0.994</u> | <u>0.008</u> |
|  | LRTFR       | 34.597        | 0.925        | 0.032        | 38.807        | 0.967        | 0.020        | 41.587        | 0.982        | 0.014        | 44.254        | 0.989        | 0.011        |
|  | NO-CTR      | <b>38.147</b> | <b>0.972</b> | <b>0.022</b> | <b>42.971</b> | <b>0.990</b> | <b>0.012</b> | <b>46.456</b> | <b>0.995</b> | <b>0.008</b> | <b>49.157</b> | <b>0.998</b> | <b>0.006</b> |
|  | Observation | 11.332        | 0.241        | 0.278        | 11.573        | 0.277        | 0.270        | 11.826        | 0.314        | 0.263        | 12.085        | 0.351        | 0.255        |
|  | TR-ALS      | 25.245        | 0.746        | 0.056        | 29.733        | 0.881        | 0.033        | 33.762        | 0.932        | 0.021        | 35.000        | 0.943        | 0.018        |
|  | SIREN       | 31.916        | 0.915        | 0.026        | 37.259        | 0.974        | 0.014        | 42.048        | 0.988        | 0.008        | 45.306        | 0.995        | 0.006        |
|  | MFN         | 28.157        | 0.802        | 0.040        | 34.213        | 0.922        | 0.020        | 38.931        | 0.969        | 0.012        | 42.759        | 0.987        | 0.007        |
|  | FR-INR      | 32.818        | 0.919        | <u>0.023</u> | <u>39.103</u> | 0.975        | <u>0.011</u> | <u>43.359</u> | <u>0.989</u> | <u>0.007</u> | <u>46.464</u> | <u>0.996</u> | <u>0.005</u> |
|  | LRTFR       | 31.836        | <u>0.928</u> | 0.026        | 37.661        | 0.975        | 0.013        | 40.447        | 0.986        | 0.010        | 43.099        | 0.991        | 0.007        |
|  | NO-CTR      | <b>35.156</b> | <b>0.980</b> | <b>0.018</b> | <b>42.294</b> | <b>0.995</b> | <b>0.008</b> | <b>46.493</b> | <b>0.998</b> | <b>0.005</b> | <b>48.878</b> | <b>0.999</b> | <b>0.004</b> |

The **best** and **second-best** results are highlighted.

TABLE II  
QUANTITATIVE RECOVERY RESULTS OF COLOR VIDEO COMPLETION

| Sampling Rate   |             | 5%            |              |              | 10%           |              |              | 15%           |              |              | 20%           |              |              |
|---|-------------|---------------|--------------|--------------|---------------|--------------|--------------|---------------|--------------|--------------|---------------|--------------|--------------|
| Color Video   | Method      | PSNR          | SSIM         | NRMSE        |
|  | Observation | 6.947         | 0.015        | 0.436        | 7.180         | 0.032        | 0.425        | 7.434         | 0.056        | 0.412        | 7.684         | 0.081        | 0.401        |
|   | TR-ALS      | 16.595        | 0.509        | 0.144        | 19.223        | 0.697        | 0.106        | 21.363        | 0.803        | 0.083        | 22.811        | 0.850        | 0.070        |
|   | SIREN       | 18.877        | 0.690        | 0.110        | 21.631        | 0.825        | 0.080        | 23.401        | 0.875        | 0.066        | <u>24.950</u> | <u>0.914</u> | <u>0.055</u> |
|   | MFN         | 17.209        | 0.583        | 0.134        | 19.180        | 0.704        | 0.107        | 21.312        | 0.807        | 0.083        | 23.153        | 0.873        | 0.068        |
|   | FR-INR      | <u>19.337</u> | <u>0.723</u> | <u>0.105</u> | <u>21.763</u> | <u>0.826</u> | <u>0.079</u> | <u>23.519</u> | <u>0.880</u> | <u>0.065</u> | 24.737        | 0.904        | 0.056        |
|   | LRTFR       | 18.340        | 0.661        | 0.118        | 20.705        | 0.777        | 0.090        | 22.437        | 0.850        | 0.073        | 23.423        | 0.870        | 0.065        |
|   | NO-CTR      | <b>19.643</b> | <b>0.765</b> | <b>0.101</b> | <b>22.030</b> | <b>0.860</b> | <b>0.077</b> | <b>24.026</b> | <b>0.908</b> | <b>0.061</b> | <b>25.382</b> | <b>0.933</b> | <b>0.052</b> |
|  | Observation | 3.895         | 0.007        | 0.676        | 4.128         | 0.013        | 0.658        | 4.375         | 0.019        | 0.639        | 4.641         | 0.025        | 0.620        |
|   | TR-ALS      | 22.867        | 0.692        | 0.076        | 25.656        | 0.803        | 0.055        | 27.461        | 0.852        | 0.045        | 28.990        | 0.890        | 0.038        |
|   | SIREN       | 24.450        | 0.805        | 0.063        | 27.119        | <u>0.879</u> | 0.047        | 29.072        | 0.908        | 0.037        | 30.715        | 0.931        | 0.031        |
|   | MFN         | 22.931        | 0.717        | 0.076        | 25.043        | 0.787        | 0.059        | 26.719        | 0.848        | 0.049        | 29.456        | 0.900        | 0.036        |
|   | FR-INR      | <u>24.955</u> | <u>0.816</u> | <u>0.060</u> | <u>27.665</u> | 0.878        | <u>0.044</u> | <u>29.711</u> | <u>0.910</u> | <u>0.035</u> | <u>31.421</u> | <u>0.935</u> | <u>0.028</u> |
|   | LRTFR       | 24.712        | 0.789        | 0.062        | 27.267        | 0.862        | 0.046        | 28.818        | 0.895        | 0.038        | 29.853        | 0.914        | 0.034        |
|   | NO-CTR      | <b>26.759</b> | <b>0.891</b> | <b>0.049</b> | <b>29.719</b> | <b>0.940</b> | <b>0.035</b> | <b>31.841</b> | <b>0.957</b> | <b>0.027</b> | <b>32.940</b> | <b>0.967</b> | <b>0.024</b> |
|  | Observation | 7.219         | 0.011        | 0.425        | 7.451         | 0.025        | 0.414        | 7.699         | 0.043        | 0.402        | 7.978         | 0.063        | 0.389        |
|   | TR-ALS      | 23.944        | 0.882        | 0.062        | 26.024        | 0.918        | 0.049        | 28.047        | 0.946        | 0.039        | 29.172        | 0.954        | 0.034        |
|   | SIREN       | 25.705        | 0.911        | 0.051        | 27.739        | 0.942        | 0.040        | 29.193        | 0.957        | 0.034        | 30.444        | 0.964        | 0.029        |
|   | MFN         | 24.984        | 0.899        | 0.055        | 26.897        | 0.927        | 0.044        | 28.632        | 0.944        | 0.036        | 30.012        | 0.964        | 0.031        |
|   | FR-INR      | 26.384        | 0.928        | 0.047        | 28.326        | 0.946        | 0.037        | 29.831        | 0.958        | 0.031        | <u>31.117</u> | 0.970        | <u>0.027</u> |
|   | LRTFR       | <u>26.766</u> | <u>0.932</u> | <u>0.045</u> | <u>28.622</u> | <u>0.954</u> | <u>0.036</u> | <u>30.228</u> | <u>0.966</u> | <u>0.030</u> | 30.983        | 0.971        | 0.028        |
|   | NO-CTR      | <b>27.459</b> | <b>0.949</b> | <b>0.041</b> | <b>29.504</b> | <b>0.966</b> | <b>0.033</b> | <b>30.849</b> | <b>0.976</b> | <b>0.028</b> | <b>32.075</b> | <b>0.981</b> | <b>0.024</b> |

The **best** and **second-best** results are highlighted.

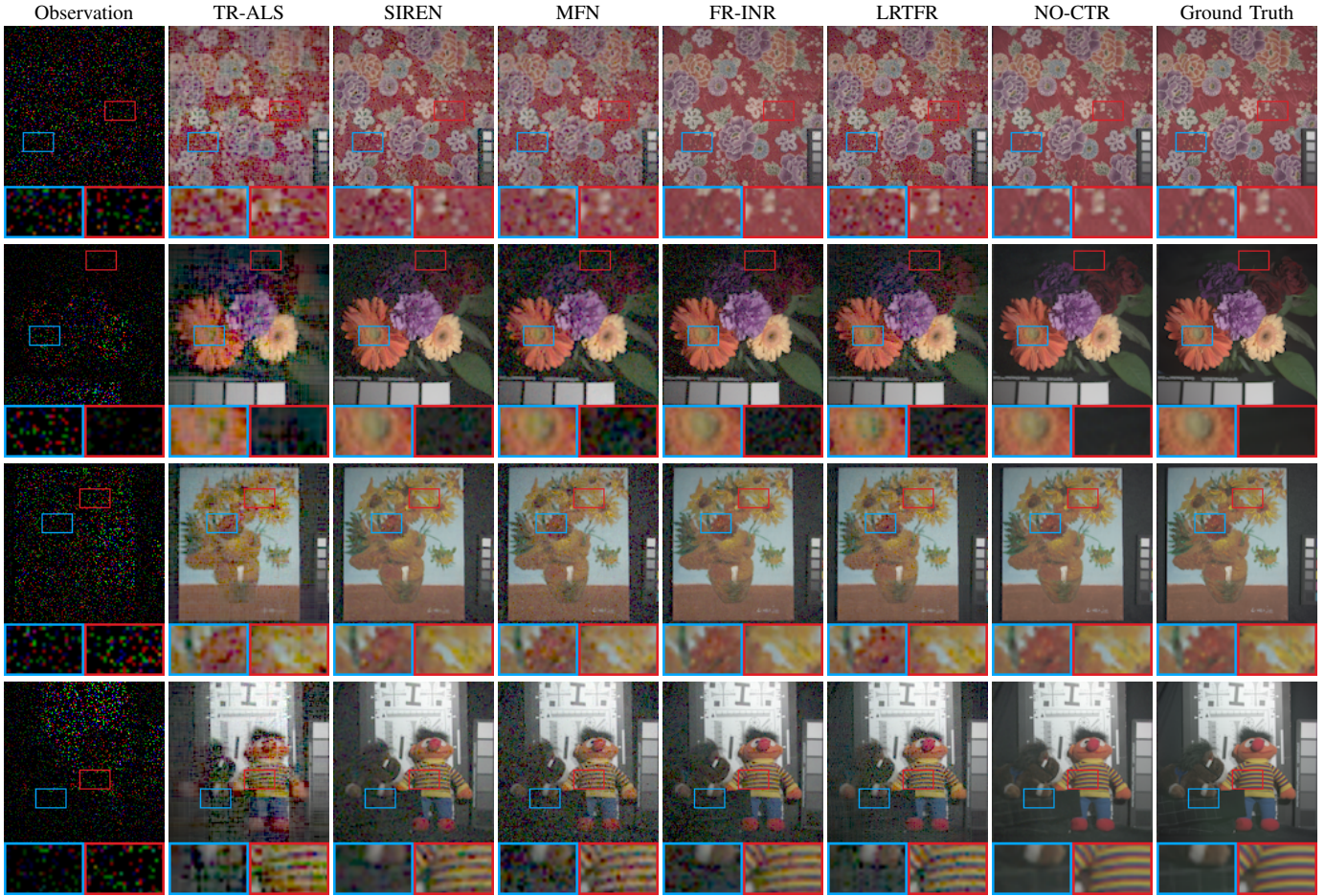


Fig. 4. Visual recovery results of MSI completion at a sampling rate of 10%.

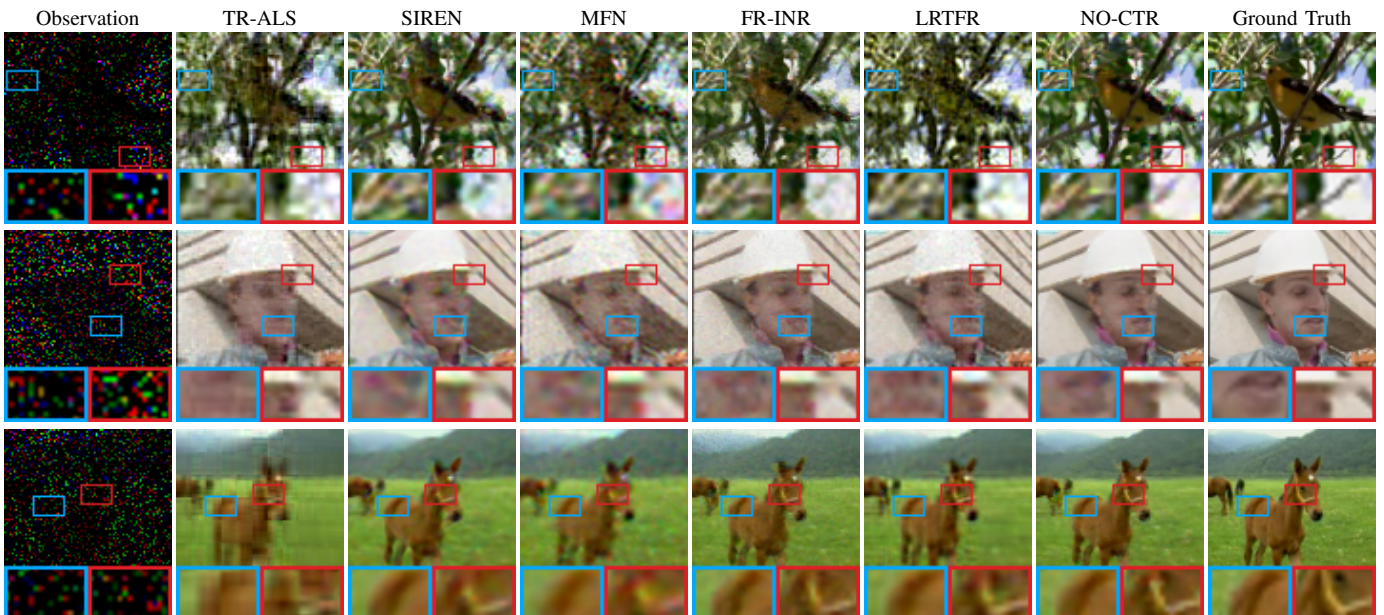


Fig. 5. Visual recovery results of color video completion at a sampling rate of 10%.

TABLE III  
QUANTITATIVE RECOVERY RESULTS OF SENTINEL-2 IMAGE COMPLETION

| Sampling Rate   |             | 5%            |              |              | 10%           |              |              | 15%           |              |              | 20%           |              |              |
|---|-------------|---------------|--------------|--------------|---------------|--------------|--------------|---------------|--------------|--------------|---------------|--------------|--------------|
| Dataset   | Method      | PSNR          | SSIM         | NRMSE        |
|  | Observation | 9.512         | 0.015        | 0.454        | 9.746         | 0.022        | 0.443        | 9.998         | 0.027        | 0.430        | 10.267        | 0.031        | 0.417        |
|   | TR-ALS      | 25.993        | 0.508        | 0.082        | 29.151        | 0.567        | 0.071        | 30.638        | 0.688        | 0.059        | 32.071        | 0.705        | 0.057        |
|   | SIREN       | 32.382        | 0.715        | 0.056        | 33.999        | 0.770        | 0.049        | 35.197        | 0.834        | 0.038        | 36.280        | 0.862        | 0.036        |
|   | MFN         | 32.202        | 0.734        | 0.058        | 33.814        | 0.800        | 0.046        | 34.967        | 0.848        | 0.039        | 35.904        | 0.871        | 0.034        |
|   | FR-INR      | <b>33.243</b> | <u>0.777</u> | <u>0.050</u> | <u>34.673</u> | <u>0.833</u> | <u>0.041</u> | <u>35.288</u> | <u>0.868</u> | <u>0.035</u> | <u>36.499</u> | <u>0.890</u> | 0.031        |
|   | LRTFR       | 30.534        | 0.706        | 0.060        | 32.039        | 0.809        | 0.043        | 33.240        | 0.861        | 0.036        | 34.227        | 0.882        | <u>0.031</u> |
|   | NO-CTR      | <u>33.206</u> | <b>0.822</b> | <b>0.045</b> | <b>35.231</b> | <b>0.873</b> | <b>0.037</b> | <b>36.389</b> | <b>0.900</b> | <b>0.032</b> | <b>37.077</b> | <b>0.916</b> | <b>0.029</b> |
|  | Observation | 8.587         | 0.014        | 0.485        | 8.819         | 0.019        | 0.472        | 9.078         | 0.024        | 0.458        | 9.340         | 0.028        | 0.445        |
|   | TR-ALS      | 22.935        | 0.461        | 0.101        | 27.835        | 0.608        | 0.061        | 30.139        | 0.696        | 0.051        | 31.615        | 0.691        | 0.045        |
|   | SIREN       | 32.530        | 0.698        | 0.052        | 33.839        | 0.790        | 0.039        | 34.834        | 0.821        | 0.036        | 36.026        | 0.858        | <u>0.027</u> |
|   | MFN         | 31.518        | 0.726        | 0.053        | 33.345        | 0.796        | 0.041        | 34.575        | 0.844        | 0.036        | 35.604        | 0.878        | 0.030        |
|   | FR-INR      | <u>32.974</u> | <u>0.792</u> | <u>0.043</u> | <u>34.507</u> | <u>0.849</u> | <u>0.036</u> | <u>35.381</u> | <u>0.874</u> | <u>0.031</u> | <u>36.299</u> | <u>0.891</u> | 0.028        |
|   | LRTFR       | 30.111        | 0.745        | 0.047        | 31.740        | 0.824        | 0.037        | 33.043        | 0.859        | 0.033        | 33.971        | 0.884        | 0.029        |
|   | NO-CTR      | <b>33.068</b> | <b>0.829</b> | <b>0.040</b> | <b>35.100</b> | <b>0.886</b> | <b>0.031</b> | <b>36.287</b> | <b>0.911</b> | <b>0.027</b> | <b>36.971</b> | <b>0.928</b> | <b>0.024</b> |
|  | Observation | 8.883         | 0.015        | 0.479        | 9.118         | 0.021        | 0.467        | 9.357         | 0.026        | 0.454        | 9.633         | 0.032        | 0.440        |
|   | TR-ALS      | 24.291        | 0.509        | 0.085        | 27.084        | 0.573        | 0.061        | 29.234        | 0.660        | 0.053        | 31.625        | 0.707        | 0.044        |
|   | SIREN       | 32.547        | 0.765        | <u>0.043</u> | 34.807        | 0.833        | <u>0.033</u> | <u>36.176</u> | 0.867        | <u>0.027</u> | <u>37.280</u> | 0.882        | <u>0.023</u> |
|   | MFN         | 31.761        | 0.769        | 0.050        | 33.921        | 0.839        | 0.038        | 34.898        | 0.869        | 0.033        | 36.537        | 0.901        | 0.027        |
|   | FR-INR      | <u>33.329</u> | <u>0.820</u> | 0.043        | <u>34.955</u> | <u>0.871</u> | 0.033        | 35.812        | <u>0.897</u> | 0.027        | 36.937        | 0.908        | 0.024        |
|   | LRTFR       | 30.691        | 0.797        | 0.044        | 32.433        | 0.846        | 0.036        | 33.681        | 0.884        | 0.030        | 34.611        | <u>0.909</u> | 0.026        |
|   | NO-CTR      | <b>33.673</b> | <b>0.879</b> | <b>0.036</b> | <b>35.892</b> | <b>0.920</b> | <b>0.028</b> | <b>37.136</b> | <b>0.938</b> | <b>0.024</b> | <b>38.100</b> | <b>0.946</b> | <b>0.021</b> |

The **best** and second-best results are highlighted.

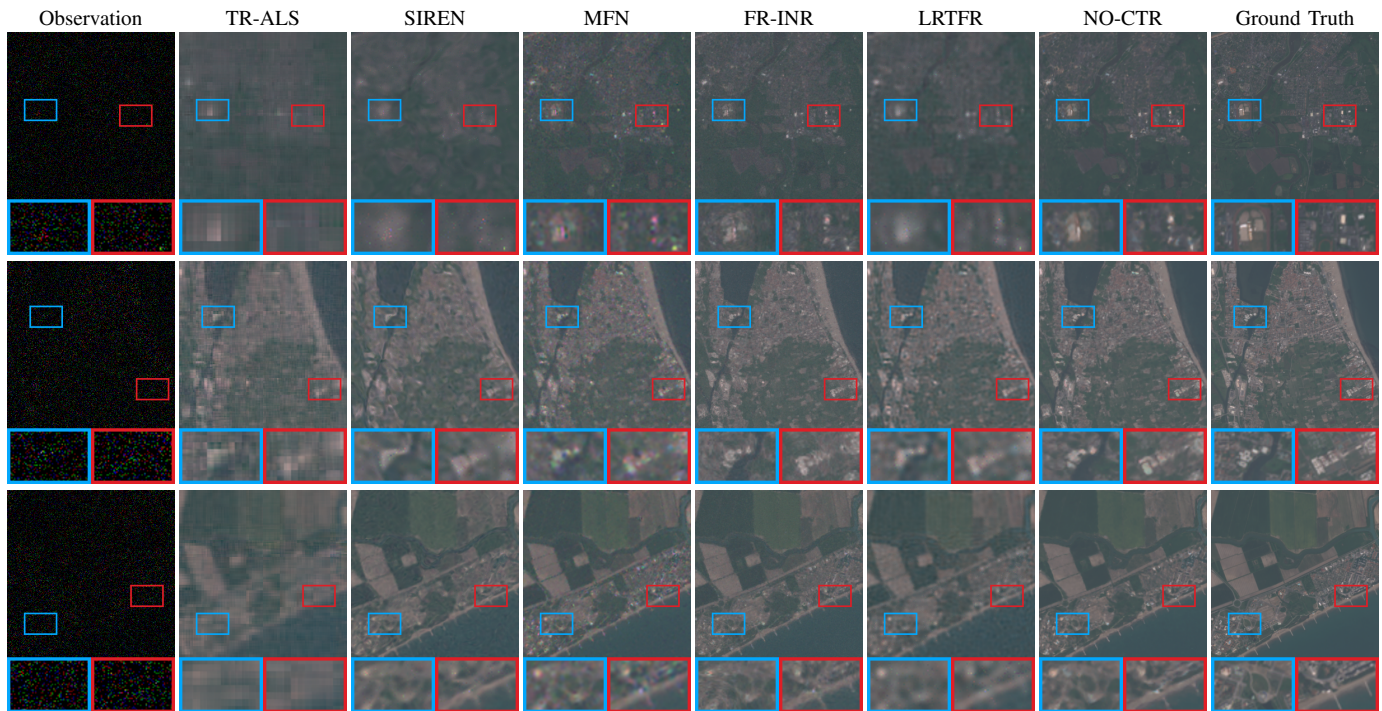


Fig. 6. Visual recovery results of Sentinel-2 image completion at a sampling rate of 10%.

TABLE IV  
QUANTITATIVE RECOVERY RESULTS OF POINT CLOUD COMPLETION

| Sampling Rate  |             | 5%           |              | 10%          |              | 15%          |              | 20%          |              |
|--|-------------|--------------|--------------|--------------|--------------|--------------|--------------|--------------|--------------|
| Point Cloud  | Method      | NRMSE        | $R^2$        | NRMSE        | $R^2$        | NRMSE        | $R^2$        | NRMSE        | $R^2$        |
| <br><i>Frog</i>   | Observation | 0.470        | -3.120       | 0.457        | -2.894       | 0.443        | -2.662       | 0.432        | -2.484       |
|  | SIREN       | <u>0.054</u> | <u>0.947</u> | 0.044        | <u>0.964</u> | <u>0.039</u> | <u>0.972</u> | <u>0.031</u> | <u>0.983</u> |
|  | MFN         | 0.060        | <u>0.936</u> | 0.051        | <u>0.953</u> | <u>0.047</u> | <u>0.959</u> | <u>0.038</u> | <u>0.974</u> |
|  | FR-INR      | 0.057        | 0.940        | 0.047        | 0.959        | 0.043        | 0.966        | 0.033        | 0.980        |
|  | LRTFR       | 0.062        | 0.930        | 0.054        | 0.947        | 0.050        | 0.955        | 0.040        | 0.971        |
|  | NO-CTR      | <b>0.051</b> | <b>0.953</b> | <b>0.041</b> | <b>0.969</b> | <b>0.034</b> | <b>0.980</b> | <b>0.028</b> | <b>0.985</b> |
| <br><i>Mario</i>  | Observation | 0.435        | -1.939       | 0.423        | -1.788       | 0.412        | -1.637       | 0.398        | -1.469       |
|  | SIREN       | <u>0.088</u> | <u>0.878</u> | <u>0.063</u> | <u>0.938</u> | <u>0.058</u> | <u>0.948</u> | <u>0.044</u> | <u>0.970</u> |
|  | MFN         | 0.096        | 0.855        | 0.069        | 0.925        | <u>0.067</u> | 0.931        | <u>0.052</u> | <u>0.957</u> |
|  | FR-INR      | 0.091        | 0.871        | 0.064        | 0.936        | 0.062        | 0.940        | 0.045        | 0.968        |
|  | LRTFR       | 0.099        | 0.846        | 0.077        | 0.906        | 0.074        | 0.915        | 0.056        | 0.951        |
|  | NO-CTR      | <b>0.083</b> | <b>0.892</b> | <b>0.061</b> | <b>0.942</b> | <b>0.055</b> | <b>0.952</b> | <b>0.043</b> | <b>0.971</b> |
| <br><i>Rabbit</i> | Observation | 0.465        | -8.562       | 0.451        | -8.003       | 0.439        | -7.546       | 0.427        | -7.077       |
|  | SIREN       | <u>0.082</u> | <u>0.709</u> | <u>0.069</u> | <u>0.795</u> | <u>0.056</u> | <u>0.863</u> | <u>0.045</u> | <u>0.914</u> |
|  | MFN         | 0.088        | 0.669        | 0.071        | 0.781        | 0.060        | 0.840        | 0.048        | 0.903        |
|  | FR-INR      | 0.095        | 0.604        | 0.070        | 0.783        | 0.058        | 0.851        | 0.046        | 0.908        |
|  | LRTFR       | 0.088        | 0.671        | 0.075        | 0.756        | 0.064        | 0.818        | 0.054        | 0.874        |
|  | NO-CTR      | <b>0.077</b> | <b>0.740</b> | <b>0.062</b> | <b>0.831</b> | <b>0.047</b> | <b>0.906</b> | <b>0.040</b> | <b>0.930</b> |

The **best** and second-best results are highlighted.

all experimental settings. With a minor exception—at 5% sampling rate on *T30UYV*, FR-INR achieves a marginally higher PSNR. Notably, this superiority becomes more pronounced as the sampling rates increase, demonstrating its strong ability for Sentinel-2 image completion. Figure 6 shows the visual recovery results of Sentinel-2 image completion when the sampling rates are 10%. Proposed NO-CTR exhibits superior capability in recovering geographical details. When reconstructing satellite images, proposed NO-CTR recovers more accurate textures and boundaries for urban structures and land cover regions, which is vital for remote sensing analyses.

#### D. Point Clouds

Finally, we conduct experiments on multi-dimensional data beyond mesh grids: point clouds, which can hardly be achieved by traditional tensor completion models. Point clouds are widely used in various fields, including computer-aided design, virtual reality, and autonomous driving, to represent the shape or surface characteristics of objects or environments. Each point cloud refers to a collection of points in three-dimensional space, where each point contains spatial coordinates and RGB values. In our experiments, each point cloud contains about 20 000 points. We random select 5%, 10%, 15%, or 20% of the points as the observation respectively, and recover the RGB values at the remaining points based on their coordinates.

Table IV lists the quantitative recovery results of point cloud completion. Proposed NO-CTR method consistently outperforms all competing methods across all point clouds and all sampling rates, as indicated by the lowest NRMSE and highest  $R^2$  in every experimental setting. Notably, this superiority holds even at both low and high sampling rates, demonstrating its effectiveness for point cloud completion. Figure 7 shows the visual recovery results of point cloud completion when the sampling rates are 10%. Proposed NO-CTR successfully reconstructs the surface details of these 3D models. The point

clouds recovered by proposed NO-CTR contain more accurate details, especially in capturing distinctive features.

## VII. DISCUSSION

### A. Contribution of Continuous and Nonlinear Mode- $n$ Operators

The continuous and nonlinear mode- $n$  operators are the heart of the NO-CTR. To discuss the contribution of continuous and nonlinear mode- $n$  operators, in this subsection, we consider different operators, including discrete and linear mode- $n$  operators, and continuous and nonlinear mode- $n$  operators. Table V lists the quantitative recovery results of MSI completion with different operators. It is obvious that continuous and nonlinear mode- $n$  operators play a huge role in improving the representation capabilities of NO-CTR, achieving more powerful representation capabilities. Compared with the previous methods with discrete and linear mode- $n$  operators, proposed NO-CTR with continuous and nonlinear mode- $n$  operators demonstrates significant advantages.

TABLE V  
QUANTITATIVE RECOVERY RESULTS OF MSI COMPLETION WITH DIFFERENT MODE- $n$  OPERATORS

| Sampling Rate  |                        | 10%           |              | 20%           |              |
|----------------|------------------------|---------------|--------------|---------------|--------------|
| MSI            | Mode- $n$ Operators    | PSNR          | SSIM         | PSNR          | SSIM         |
| <i>Flowers</i> | No Operator            | 30.565        | 0.898        | 34.367        | 0.948        |
|                | Discrete & Linear      | 39.175        | 0.984        | 43.119        | 0.984        |
|                | Continuous & Nonlinear | <b>42.591</b> | <b>0.994</b> | <b>49.717</b> | <b>0.999</b> |
| <i>Toy</i>     | No Operator            | 26.190        | 0.835        | 29.087        | 0.895        |
|                | Discrete & Linear      | 38.907        | 0.982        | 41.395        | 0.991        |
|                | Continuous & Nonlinear | <b>42.294</b> | <b>0.995</b> | <b>48.878</b> | <b>0.999</b> |

The **best** results are highlighted.

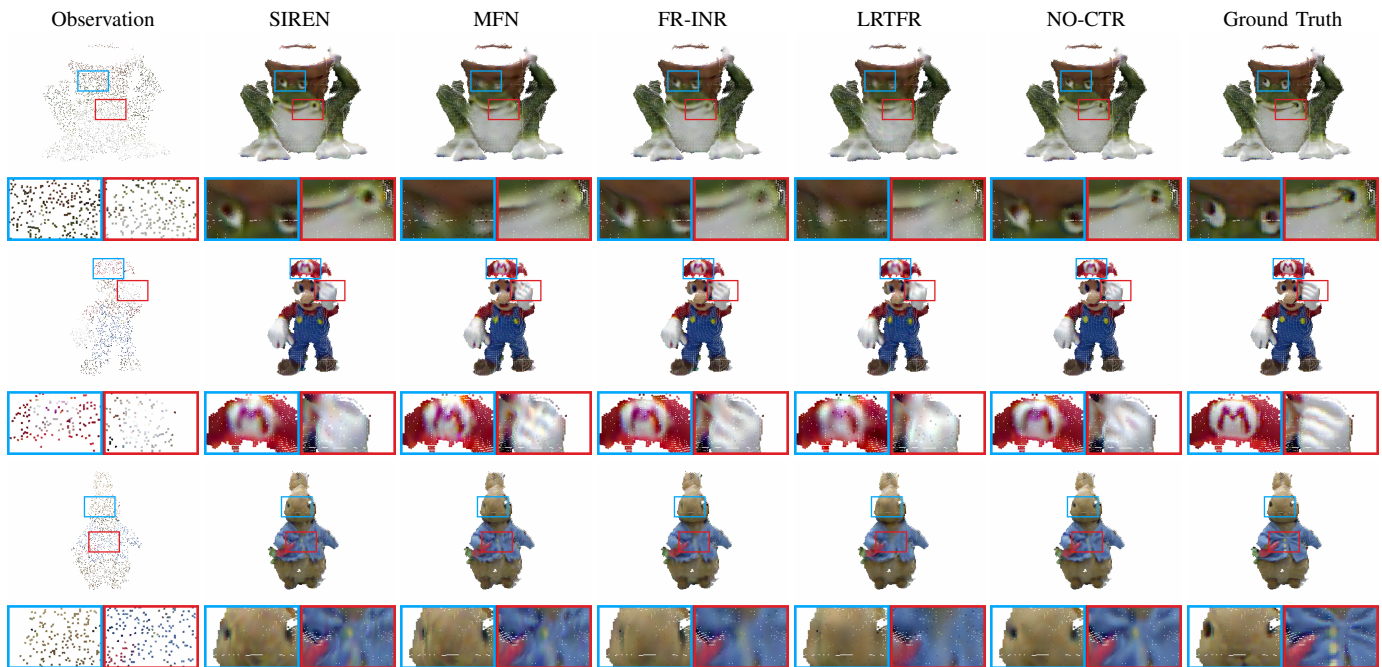


Fig. 7. Visual recovery results of point cloud completion at a sampling rate of 10%.

### B. Architectures of Neural Operators

In NO-CTR, the continuous and nonlinear mode- $n$  operators can be elegantly deployed with neural operators, which directly map the continuous core tensor function to the continuous target tensor function. To discuss the influence of neural operators, in this subsection, we consider two popular neural operators: Fourier neural operators (FNO) [37] and deep operator networks (DeepONet) [36]. Table VI lists the quantitative recovery results of MSI completion with different neural operators. Neural operators indeed enhance the performance of the NO-CTR, and DeepONet achieves better performance due to its flexible architecture.

TABLE VI  
QUANTITATIVE RECOVERY RESULTS OF MSI COMPLETION WITH DIFFERENT NEURAL OPERATORS

| Sampling Rate  |              | 10%           |              | 20%           |              |
|----------------|--------------|---------------|--------------|---------------|--------------|
| MSI            | Architecture | PSNR          | SSIM         | PSNR          | SSIM         |
| <i>Flowers</i> | No Operator  | 30.565        | 0.898        | 34.367        | 0.948        |
|                | FNO          | 40.940        | 0.992        | 47.446        | 0.997        |
|                | DeepONet     | <b>42.591</b> | <b>0.994</b> | <b>49.717</b> | <b>0.999</b> |
| <i>Toy</i>     | No Operator  | 26.190        | 0.835        | 29.087        | 0.895        |
|                | FNO          | 41.167        | 0.994        | 46.076        | 0.998        |
|                | DeepONet     | <b>42.294</b> | <b>0.995</b> | <b>48.878</b> | <b>0.999</b> |

The **best** results are highlighted.

### C. Influence of Continuous Core Tensor Function

The continuous core tensor function is also an important element of the NO-CTR. In this subsection, we discuss the influence of the continuous core tensor function. Here we consider different representation methods for the continuous core tensor function, including LRTFR [34], positional encoding-based multi-layer perceptron (referred to as PE-MLP) [41],

and SIREN [40]. Table VII list the quantitative recovery results of MSI completion with different representation methods for the continuous core tensor function. LRTFR imposes low-rank constraints on the continuous core tensor functions, which limits its representation capability to some extent. SIREN demonstrates the best performance here.

TABLE VII  
QUANTITATIVE RECOVERY RESULTS OF MSI COMPLETION WITH DIFFERENT REPRESENTATION METHODS FOR THE CONTINUOUS CORE TENSOR FUNCTION

| Sampling Rate  |        | 10%           |              | 20%           |              |
|----------------|--------|---------------|--------------|---------------|--------------|
| MSI            | Core   | PSNR          | SSIM         | PSNR          | SSIM         |
| <i>Flowers</i> | LRTFR  | 39.586        | 0.983        | 44.232        | 0.992        |
|                | PE-MLP | 42.086        | 0.993        | 47.326        | 0.998        |
|                | SIREN  | <b>42.591</b> | <b>0.994</b> | <b>49.717</b> | <b>0.999</b> |
| <i>Toy</i>     | LRTFR  | 37.781        | 0.980        | 41.948        | 0.991        |
|                | PE-MLP | 40.831        | 0.993        | 45.765        | 0.998        |
|                | SIREN  | <b>42.294</b> | <b>0.995</b> | <b>48.878</b> | <b>0.999</b> |

The **best** results are highlighted.

### D. Number of Learnable Parameters

In this subsection, we compare the number of learnable parameters among different continuous tensor function representations, including SIREN [40], LRTFR [34], and proposed NO-CTR. The number of learnable parameters is a key indicator of model complexity, and is also related to training costs and speed. The proposed NO-CTR has the largest number of parameters, as it involves a continuous core tensor function and a series of neural operator-based continuous and nonlinear mode- $n$  operators. Despite having more parameters, NO-CTR achieves significantly better recovery performance. This indicates that the increase in parameters is reasonable and effective.

TABLE VIII  
QUANTITATIVE RECOVERY RESULTS AND NUMBER OF PARAMETERS OF  
MSI COMPLETION WITH DIFFERENT CONTINUOUS TENSOR FUNCTION  
REPRESENTATIONS

| Sampling Rate |        | 10%           |              |               | 20%           |              |               |
|---------------|--------|---------------|--------------|---------------|---------------|--------------|---------------|
| MSI           | Method | PSNR          | SSIM         | Parameters    | PSNR          | SSIM         | Parameters    |
| Flowers       | SIREN  | 38.681        | 0.977        | <b>16 711</b> | 46.041        | 0.995        | <b>47 671</b> |
|               | LRTFR  | 36.879        | 0.965        | 130 191       | 43.249        | 0.991        | 331 023       |
|               | NO-CTR | <b>42.591</b> | <b>0.994</b> | 507 341       | <b>49.717</b> | <b>0.999</b> | 472 721       |
| Toy           | SIREN  | 37.259        | 0.974        | <b>16 711</b> | 45.306        | 0.995        | <b>47 671</b> |
|               | LRTFR  | 37.661        | 0.975        | 130 191       | 43.099        | 0.991        | 595 231       |
|               | NO-CTR | <b>42.294</b> | <b>0.995</b> | 597 791       | <b>48.878</b> | <b>0.999</b> | 599 291       |

The best results are highlighted.

### E. Hyper-Parameter Sensitivity

In this subsection, we discuss the hyper-parameter sensitivity. We focus on the heart of the NO-CTR: continuous and nonlinear mode- $n$  operators. The continuous and nonlinear mode- $n$  operators are elegantly deployed with DeepONets [36]. Specifically, for each inducing operator in Equation (4),

$$F_n(v)(y) = \sum_{p=1}^{P_n} b_p^{(n)}(v(z_1), v(z_2), \dots, v(z_{m_n})) t_p^{(n)}(y), \quad (6)$$

where  $v \in C([0, 1])$  is the input function,  $y \in [0, 1]$  is a coordinate,  $\{b_p^{(n)}\}_{p=1}^{P_n}$  are scalar-valued functions called branch networks,  $t^{(n)}$  is a vector-valued function called trunk network,  $\{t_p^{(n)}\}_{p=1}^{P_n}$  are  $P_n$  components of  $t^{(n)}$ , and  $z_i \in [0, 1]$  ( $i = 1, 2, \dots, m_n$ ) are fixed location called sensors. Here we consider two hyper-parameters in DeepONet: the number of sensors  $m_n$  and the number of branch networks  $P_n$ .

1) *Number of Sensors*: DeepONet requires the input function values at a sufficient but finite number of locations (i.e.  $\{z_i\}_{i=1}^{m_n}$  in Equation (6)) and these locations are called “sensors”. The number of sensors (i.e.  $m_n$  in Equation (6)) directly determines the accuracy and information of the input of DeepONet. Figure 8 shows the quantitative recovery results w.r.t. different numbers of sensors. As the number of sensors increases, both PSNR and SSIM values first rise sharply; after that, they exhibit a stable trend with slight fluctuations, implying that a proper number of sensors is sufficient to achieve favorable recovery performance.

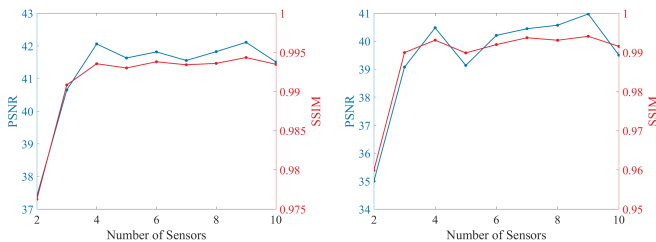


Fig. 8. Quantitative recovery results w.r.t. different numbers of sensors on the MSIs *Flowers* (left) and *Toy* (right) at a sampling rate of 10%.

2) *Number of Branch Networks*: DeepONet consist of a trunk network and several branch networks. These branch networks are mainly used to handle the input function. According to [36], using lots of branch networks is inefficient, so all the

branch networks are merged into one single neural network, which can be viewed as all the branch networks sharing the same set of parameters. The number of branch networks (i.e.  $P_n$  in Equation (6)) is the output dimension of this neural network. Figure 9 shows the quantitative recovery results w.r.t. different numbers of branch networks. The results show that both PSNR and SSIM values initially rise with an increasing number of branches, reaching an optimal range. Beyond this point, further expanding the branch networks leads to slight fluctuations.

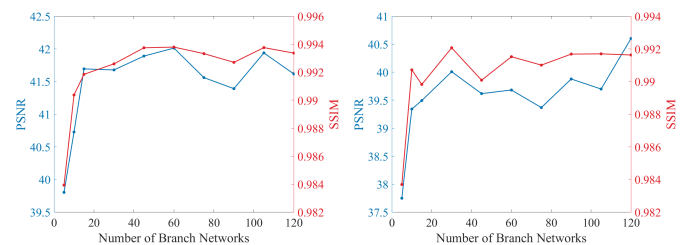


Fig. 9. Quantitative recovery results w.r.t. different numbers of branch networks on the MSIs *Flowers* (left) and *Toy* (right) at a sampling rate of 10%.

## VIII. CONCLUSION

To unlock the potential of continuous tensor function representations, in this paper, we first suggested neural operator-grounded mode- $n$  operators as a continuous and nonlinear alternative, which provides a genuine continuous representation of real-world data and can ameliorate discretization artifacts. Empowering with continuous and nonlinear mode- $n$  operators, we proposed a neural operator-grounded continuous tensor function representation (abbreviated as NO-CTR), which can more faithfully represent complex real-world data compared with classic discrete tensor representations and continuous tensor function representations. Theoretically, we also proved that any continuous tensor function can be approximated by NO-CTR. To examine the capability of NO-CTR, we suggested an NO-CTR-based multi-dimensional data completion model. Extensive experiments across various data on regular mesh grids (multi-spectral images and color videos), on mesh grids with different resolutions (Sentinel-2 images) and beyond mesh grids (point clouds) demonstrated the superiority of NO-CTR.

## REFERENCES

- [1] J. Hou, F. Zhang, H. Qiu, J. Wang, Y. Wang, and D. Meng, “Robust low-tubal-rank tensor recovery from binary measurements,” *IEEE Transactions on Pattern Analysis and Machine Intelligence*, vol. 44, no. 8, pp. 4355–4373, 2022.
- [2] X. Chen and L. Sun, “Bayesian temporal factorization for multidimensional time series prediction,” *IEEE Transactions on Pattern Analysis and Machine Intelligence*, vol. 44, no. 9, pp. 4659–4673, 2022.
- [3] H. Wang, J. Peng, W. Qin, J. Wang, and D. Meng, “Guaranteed tensor recovery fused low-rankness and smoothness,” *IEEE Transactions on Pattern Analysis and Machine Intelligence*, vol. 45, no. 9, pp. 10990–11 007, 2023.
- [4] C. He, Y. Xu, Z. Wu, S. Zheng, and Z. Wei, “Multi-dimensional visual data restoration: Uncovering the global discrepancy in transformed high-order tensor singular values,” *IEEE Transactions on Image Processing*, vol. 33, pp. 6409–6424, 2024.

- [5] W. He, Q. Yao, C. Li, N. Yokoya, Q. Zhao, H. Zhang, and L. Zhang, "Non-local meets global: An iterative paradigm for hyperspectral image restoration," *IEEE Transactions on Pattern Analysis and Machine Intelligence*, vol. 44, no. 4, pp. 2089–2107, 2022.
- [6] T.-H. Zhang, J.-L. Zhao, S. Fang, Z. Li, and M.-G. Gong, "Full-mode-augmentation tensor-train rank minimization for hyperspectral image inpainting," *IEEE Transactions on Geoscience and Remote Sensing*, vol. 62, pp. 1–13, 2024.
- [7] S. Li, Z. Zhou, M. Zhao, J. Yang, W. Guo, Y. Lv, L. Kou, H. Wang, and Y. Gu, "A multitask benchmark dataset for satellite video: Object detection, tracking, and segmentation," *IEEE Transactions on Geoscience and Remote Sensing*, vol. 61, pp. 1–21, 2023.
- [8] K. Wang, M. Zhou, Q. Lin, G. Niu, and X. Zhang, "Geometry-guided point generation for 3D object detection," *IEEE Signal Processing Letters*, vol. 32, pp. 136–140, 2025.
- [9] B.-Z. Fu, T.-Z. Huang, X.-L. Zhao, W.-H. Wu, and H. Peng, "ProTD: Prompted tensor decomposition for hyperspectral anomaly detection," *IEEE Transactions on Geoscience and Remote Sensing*, vol. 63, pp. 1–13, 2025.
- [10] X. Zhang and M. K. Ng, "Low rank tensor completion with poisson observations," *IEEE Transactions on Pattern Analysis and Machine Intelligence*, vol. 44, no. 8, pp. 4239–4251, 2022.
- [11] J. Jiang, Y. Xu, H. Xu, G. Shen, and J. Zheng, "Multi-dimensional visual data completion via weighted hybrid graph-Laplacian," *Signal Processing*, vol. 216, p. 109305, 2024.
- [12] R. Su, X.-L. Zhao, W.-H. Wu, S. Liu, and J. He, "Deep fully-connected tensor network decomposition for multi-dimensional signal recovery," *Signal Processing*, vol. 233, p. 109903, 2025.
- [13] M. M. Salut and D. V. Anderson, "Randomized tensor robust PCA for noisy hyperspectral image classification," *IEEE Geoscience and Remote Sensing Letters*, vol. 20, pp. 1–5, 2023.
- [14] R. Zhang, Z. Rong, and Z. Dong, "CAMGnet: A self-learning classification model for univariate continuous time series signals via dynamic fusion of multi-dimensional cross-domain features," *Neurocomputing*, vol. 657, p. 131686, 2025.
- [15] C. Zhu, G. Lu, B. He, R. Xie, and L. Song, "Implicit-explicit integrated representations for multi-view video compression," *IEEE Transactions on Image Processing*, vol. 34, pp. 1106–1118, 2025.
- [16] C. Shi, K. Shi, Z. Zeng, and F. Zhu, "Dynamic feature enhancement network guided by multi-dimensional collaborative edge information for remote sensing image compression," *Knowledge-Based Systems*, vol. 310, p. 112996, 2025.
- [17] Q. Xie, Q. Zhao, D. Meng, and Z. Xu, "Kronecker-basis-representation based tensor sparsity and its applications to tensor recovery," *IEEE Transactions on Pattern Analysis and Machine Intelligence*, vol. 40, no. 8, pp. 1888–1902, 2018.
- [18] F. Zhang, J. Wang, W. Wang, and C. Xu, "Low-tubal-rank plus sparse tensor recovery with prior subspace information," *IEEE Transactions on Pattern Analysis and Machine Intelligence*, vol. 43, no. 10, pp. 3492–3507, 2021.
- [19] J.-Y. Xie, H. Zhang, X.-L. Zhao, and Y.-S. Luo, "IRTF: A new tensor factorization for irregular multidimensional data recovery," *Knowledge-Based Systems*, vol. 330, p. 114372, 2025.
- [20] L. Xu, L. Cheng, N. Wong, and Y.-C. Wu, "To fold or not to fold: Graph regularized tensor train for visual data completion," *IEEE Transactions on Pattern Analysis and Machine Intelligence*, pp. 1–18, 2025.
- [21] E. J. Candès and B. Recht, "Exact matrix completion via convex optimization," *Foundations of Computational Mathematics*, vol. 9, pp. 717–772, 2009.
- [22] J.-F. Cai, E. J. Candès, and Z. Shen, "A singular value thresholding algorithm for matrix completion," *SIAM Journal on Optimization*, vol. 20, no. 4, pp. 1956–1982, 2010.
- [23] M. Fornasier, H. Rauhut, and R. Ward, "Low-rank matrix recovery via iteratively reweighted least squares minimization," *SIAM Journal on Optimization*, vol. 21, no. 4, pp. 1614–1640, 2011.
- [24] J. D. Carroll and J.-J. Chang, "Analysis of individual differences in multidimensional scaling via an n-way generalization of "Eckart-Young" decomposition," *Psychometrika*, vol. 35, pp. 283–319, 1970.
- [25] R. A. Harshman, "Foundations of the PARAFAC procedure: Models and conditions for an "explanatory" multimodal factor analysis," *UCLA Working Papers in Phonetics*, vol. 16, pp. 1–84, 1970.
- [26] L. R. Tucker, "Some mathematical notes on three-mode factor analysis," *Psychometrika*, vol. 31, pp. 279–311, 1966.
- [27] M. E. Kilmer, C. D. Martin, and L. Perrone, "A third-order generalization of the matrix SVD as a product of third-order tensors," Department of Computer Science, Tufts University, Medford, MA, USA, Tech. Rep. TR-2008-4, 2008.
- [28] M. E. Kilmer and C. D. Martin, "Factorization strategies for third-order tensors," *Linear Algebra and its Applications*, vol. 435, no. 3, pp. 641–658, 2011, special Issue: Dedication to Pete Stewart on the occasion of his 70th birthday.
- [29] M. E. Kilmer, K. Braman, N. Hao, and R. C. Hoover, "Third-order tensors as operators on matrices: A theoretical and computational framework with applications in imaging," *SIAM Journal on Matrix Analysis and Applications*, vol. 34, no. 1, pp. 148–172, 2013.
- [30] I. V. Oseledets, "Tensor-train decomposition," *SIAM Journal on Scientific Computing*, vol. 33, no. 5, pp. 2295–2317, 2011.
- [31] Q. Zhao, G. Zhou, S. Xie, L. Zhang, and A. Cichocki, "Tensor ring decomposition," 2016. [Online]. Available: <https://arxiv.org/abs/1606.05535>
- [32] M. Imaizumi and K. Hayashi, "Tensor decomposition with smoothness," in *Proceedings of the 34th International Conference on Machine Learning*, ser. Proceedings of Machine Learning Research, D. Precup and Y. W. Teh, Eds., vol. 70. PMLR, 06–11 Aug 2017, pp. 1597–1606.
- [33] S. Fang, X. Yu, Z. Wang, S. Li, M. Kirby, and S. Zhe, "Functional bayesian Tucker decomposition for continuous-indexed tensor data," in *The Twelfth International Conference on Learning Representations*, 2024.
- [34] Y. Luo, X. Zhao, Z. Li, M. K. Ng, and D. Meng, "Low-rank tensor function representation for multi-dimensional data recovery," *IEEE Transactions on Pattern Analysis and Machine Intelligence*, vol. 46, no. 5, pp. 3351–3369, 2024.
- [35] A. Anandkumar, K. Azizzadenesheli, K. Bhattacharya, N. Kovachki, Z. Li, B. Liu, and A. Stuart, "Neural operator: Graph kernel network for partial differential equations," in *ICLR 2020 Workshop on Integration of Deep Neural Models and Differential Equations*, 2019.
- [36] L. Lu, P. Jin, G. Pang, Z. Zhang, and G. E. Karniadakis, "Learning nonlinear operators via deepONet based on the universal approximation theorem of operators," *Nature Machine Intelligence*, vol. 3, pp. 218–229, 2021.
- [37] Z. Li, N. B. Kovachki, K. Azizzadenesheli, B. Liu, K. Bhattacharya, A. Stuart, and A. Anandkumar, "Fourier neural operator for parametric partial differential equations," in *International Conference on Learning Representations*, 2021.
- [38] J. J. Park, P. Florence, J. Straub, R. Newcombe, and S. Lovegrove, "DeepSDF: Learning continuous signed distance functions for shape representation," in *2019 IEEE/CVF Conference on Computer Vision and Pattern Recognition (CVPR)*, 2019, pp. 165–174.
- [39] L. Mescheder, M. Oechsle, M. Niemeyer, S. Nowozin, and A. Geiger, "Occupancy networks: Learning 3D reconstruction in function space," in *2019 IEEE/CVF Conference on Computer Vision and Pattern Recognition (CVPR)*, 2019, pp. 4455–4465.
- [40] W. Sitzmann, J. Martel, A. Bergman, D. Lindell, and G. Wetzstein, "Implicit neural representations with periodic activation functions," in *Advances in Neural Information Processing Systems*, H. Larochelle, M. Ranzato, R. Hadsell, M. Balcan, and H. Lin, Eds., vol. 33. Curran Associates, Inc., 2020, pp. 7462–7473.
- [41] M. Tancik, P. Srinivasan, B. Mildenhall, S. Fridovich-Keil, N. Raghavan, U. Singhal, R. Ramamoorthi, J. Barron, and R. Ng, "Fourier features let networks learn high frequency functions in low dimensional domains," in *Advances in Neural Information Processing Systems*, H. Larochelle, M. Ranzato, R. Hadsell, M. Balcan, and H. Lin, Eds., vol. 33. Curran Associates, Inc., 2020, pp. 7537–7547.
- [42] V. Saragadam, D. LeJeune, J. Tan, G. Balakrishnan, A. Veeraraghavan, and R. G. Baraniuk, "Wire: Wavelet implicit neural representations," in *2023 IEEE/CVF Conference on Computer Vision and Pattern Recognition (CVPR)*, 2023, pp. 18 507–18 516.
- [43] K. Shi, X. Zhou, and S. Gu, "Improved implicit neural representation with fourier reparameterized training," in *2024 IEEE/CVF Conference on Computer Vision and Pattern Recognition (CVPR)*, 2024, pp. 25 985–25 994.
- [44] R. Fathony, A. K. Sahu, D. Willmott, and J. Z. Kolter, "Multiplicative filter networks," in *International Conference on Learning Representations*, 2021.
- [45] Y. Chen, S. Liu, and X. Wang, "Learning continuous image representation with local implicit image function," in *2021 IEEE/CVF Conference on Computer Vision and Pattern Recognition (CVPR)*, 2021, pp. 8624–8634.
- [46] G. Yüce, G. Ortiz-Jiménez, B. Besbinar, and P. Frossard, "A structured dictionary perspective on implicit neural representations," in *2022 IEEE/CVF Conference on Computer Vision and Pattern Recognition (CVPR)*, 2022, pp. 19 206–19 216.
- [47] V. Saragadam, J. Tan, G. Balakrishnan, R. G. Baraniuk, and A. Veeraraghavan, "Miner: Multiscale implicit neural representation," in *Com-*

- puter Vision – ECCV 2022, S. Avidan, G. Brostow, M. Cissé, G. M. Farinella, and T. Hassner, Eds. Cham: Springer Nature Switzerland, 2022, pp. 318–333.
- [48] J. Li, X. Zhao, J. Wang, C. Wang, and M. Wang, “Superpixel-informed implicit neural representation for multi-dimensional data,” in *Computer Vision – ECCV 2024*, A. Leonardis, E. Ricci, S. Roth, O. Russakovsky, T. Sattler, and G. Varol, Eds. Cham: Springer Nature Switzerland, 2025, pp. 258–276.
- [49] T.-W. Zhou, X.-L. Zhao, W.-H. Wu, J.-L. Wang, and Y.-S. Luo, “Frequency-aware implicit neural representation for multi-dimensional data recovery,” *IEEE Transactions on Circuits and Systems for Video Technology*, pp. 1–1, 2025.
- [50] N. Boullé and A. Townsend, “A mathematical guide to operator learning,” in *Numerical Analysis Meets Machine Learning*, ser. Handbook of Numerical Analysis, S. Mishra and A. Townsend, Eds. Elsevier, 2024, vol. 25, pp. 83–125.
- [51] N. B. Kovachki, S. Lanthaler, and A. M. Stuart, “Operator learning: Algorithms and analysis,” in *Numerical Analysis Meets Machine Learning*, ser. Handbook of Numerical Analysis, S. Mishra and A. Townsend, Eds. Elsevier, 2024, vol. 25, pp. 419–467.
- [52] N. Kovachki, Z. Li, B. Liu, K. Azizzadenesheli, K. Bhattacharya, A. Stuart, and A. Anandkumar, “Neural operator: Learning maps between function spaces with applications to pdes,” *Journal of Machine Learning Research*, vol. 24, no. 89, pp. 1–97, 2023.
- [53] S. K. Vemuri, T. Büchner, J. Niebling, and J. Denzler, “Functional tensor decompositions for physics-informed neural networks,” in *Pattern Recognition*, A. Antonacopoulos, S. Chaudhuri, R. Chellappa, C.-L. Liu, S. Bhattacharya, and U. Pal, Eds. Cham: Springer Nature Switzerland, 2025, pp. 32–46.
- [54] T. G. Kolda and B. W. Bader, “Tensor decompositions and applications,” *SIAM Review*, vol. 51, no. 3, pp. 455–500, 2009.
- [55] W. Wang, V. Aggarwal, and S. Aeron, “Efficient low rank tensor ring completion,” in *2017 IEEE International Conference on Computer Vision (ICCV)*, 2017, pp. 5698–5706.
- [56] Z. Wang, A. Bovik, H. Sheikh, and E. Simoncelli, “Image quality assessment: from error visibility to structural similarity,” *IEEE Transactions on Image Processing*, vol. 13, no. 4, pp. 600–612, 2004.
- [57] F. Yasuma, T. Mitsunaga, D. Iso, and S. Nayar, “Generalized assorted pixel camera: Post-capture control of resolution, dynamic range and spectrum,” Tech. Rep., Nov 2008.
- [58] O. Calin, *Universal Approximators*. Cham: Springer International Publishing, 2020, pp. 251–284.
- [59] T. Chen and H. Chen, “Universal approximation to nonlinear operators by neural networks with arbitrary activation functions and its application to dynamical systems,” *IEEE Transactions on Neural Networks*, vol. 6, no. 4, pp. 911–917, 1995.

APPENDIX  
PROOF OF THEOREM 1

*Lemma 1 ([58]):* Let  $\sigma$  be any continuous discriminatory function. Then the finite sums of the form

$$\sum_{k=1}^K a_k \sigma(\mathbf{w}_k^T \mathbf{y} + b_k), \quad \mathbf{w}_k \in \mathbb{R}^N, \quad a_k, b_k \in \mathbb{R}$$

are dense in  $C([0, 1]^N)$ .

*Lemma 2 ([36], [59]):* Suppose that  $W$  is a Banach space,  $K_1 \subseteq W$  and  $K_2 \subseteq \mathbb{R}^N$  are two compact sets in  $W$  and  $\mathbb{R}^N$ , respectively,  $V$  is a compact set in  $C(K_1)$ ,  $F$  is a continuous operator, which maps  $V$  to  $C(K_2)$ . Then for any  $\varepsilon > 0$ , there are positive integers  $m$  and  $P$ , continuous functions  $b_p \in C(\mathbb{R}^m)$  and  $t_p \in C(K_2)$  implemented by deep neural networks,  $p = 1, 2, \dots, P$ ,  $\mathbf{x}_1, \mathbf{x}_2, \dots, \mathbf{x}_m \in K_1$ , such that

$$\left| F(v)(\mathbf{y}) - \sum_{p=1}^P b_p(v(\mathbf{x}_1), v(\mathbf{x}_2), \dots, v(\mathbf{x}_m)) t_p(\mathbf{y}) \right| < \varepsilon$$

holds for all  $v \in V$  and  $\mathbf{y} \in K_2$ .

*Proof of Theorem 1:* According to Lemma 1, there is a two-layer fully connected neural network

$$\mathbf{G}: [0, 1]^N \rightarrow \mathbb{R}, \quad \mathbf{y} \mapsto \sum_{k=1}^K a_k \sigma(\mathbf{w}_k^T \mathbf{y} + b_k)$$

such that

$$\|\mathbf{G} - \mathbf{X}\| < \frac{\varepsilon}{2}. \quad (7)$$

Noticing that  $\mathbf{X}$  is a continuous function defined on a compact set  $[0, 1]^N$ , so  $\mathbf{X}$  is bounded, and  $\mathbf{G}$  is also bounded. Assume that

$$\|\mathbf{G}\| \leq M. \quad (8)$$

According to Lemma 2, there are  $N$  neural operators implemented by DeepONet

$$F_n: C([0, 1]) \rightarrow C([0, 1]), \quad u(\cdot) \mapsto \sum_{p=1}^{P_n} b_p^{(n)}(u(x_1), u(x_2), \dots, u(x_{m_n})) t_p^{(n)}(\cdot),$$

such that

$$|F_n(u)(y) - I(u)(y)| < \frac{\varepsilon}{(2^{N+1} - 2)M}$$

holds for all  $u \in C([0, 1])$  and  $y \in [0, 1]$ , so

$$\begin{aligned} \|F_n - I\| &= \sup_{\|u\|=1} \|(F_n - I)(u)\| \\ &= \sup_{\|u\|=1} \|F_n(u) - I(u)\| \\ &= \sup_{\|u\|=1} \sup_{y \in [0, 1]} |(F_n(u) - I(u))(y)| \\ &= \sup_{\|u\|=1} \sup_{y \in [0, 1]} |F_n(u)(y) - I(u)(y)| \\ &\leq \frac{\varepsilon}{(2^{N+1} - 2)M}, \end{aligned}$$

where  $I$  denotes identity transform,  $n = 1, 2, \dots, N$ . Thus,

$$\begin{aligned} \|\mathcal{F}_n^{(n)} - \mathcal{J}^{(n)}\| &= \sup_{\|\mathbf{X}\|=1} \|(\mathcal{F}_n^{(n)} - \mathcal{J}^{(n)})(\mathbf{X})\| \\ &= \sup_{\|\mathbf{X}\|=1} \sup_{\mathbf{y} \in [0, 1]^N} |(\mathcal{F}_n^{(n)} - \mathcal{J}^{(n)})(\mathbf{X})(\mathbf{y})| \\ &= \sup_{\|\mathbf{X}\|=1} \sup_{\mathbf{y} \in [0, 1]^N} |(F_n - I)(\mathbf{X}(y_1, \dots, y_{n-1}, \cdot, y_{n+1}, \dots, y_N))(y_n)| \\ &= \sup_{\|\mathbf{X}\|=1} \sup_{\bar{\mathbf{y}} \in [0, 1]^{N-1}} \sup_{y_n \in [0, 1]} |(F_n - I)(\mathbf{X}(y_1, \dots, y_{n-1}, \cdot, y_{n+1}, \dots, y_N))(y_n)| \\ &= \sup_{\|\mathbf{X}\|=1} \sup_{\bar{\mathbf{y}} \in [0, 1]^{N-1}} \|(F_n - I)(\mathbf{X}(y_1, \dots, y_{n-1}, \cdot, y_{n+1}, \dots, y_N))\| \end{aligned}$$

$$\begin{aligned}
&\leq \sup_{\|\mathbf{X}\|=1} \sup_{\bar{\mathbf{y}} \in [0,1]^{N-1}} \|F_n - I\| \|\mathbf{X}(y_1, \dots, y_{n-1}, y_{n+1}, \dots, y_N)\| \\
&= \|F_n - I\| \sup_{\|\mathbf{X}\|=1} \sup_{\bar{\mathbf{y}} \in [0,1]^{N-1}} \sup_{y_n \in [0,1]} |\mathbf{X}(y_1, \dots, y_{n-1}, y_n, y_{n+1}, \dots, y_N)| \\
&= \|F_n - I\| \sup_{\|\mathbf{X}\|=1} \|\mathbf{X}\| \\
&= \|F_n - I\| \\
&\leq \frac{\varepsilon}{(2^{N+1} - 2)M}, \tag{9}
\end{aligned}$$

where  $\mathbf{y} = (y_1, y_2, \dots, y_N) \in [0, 1]^N$ ,  $\bar{\mathbf{y}} = (y_1, \dots, y_{n-1}, y_{n+1}, \dots, y_N) \in [0, 1]^{N-1}$ ,  $\mathcal{F}_n^{(n)}$  and  $\mathcal{I}^{(n)}$  are the continuous and nonlinear mode- $n$  operators induced by  $F_n$  and  $I$ , respectively. Without loss of generality, we assume that

$$\|\mathcal{F}_n^{(n)}\| \leq 2. \tag{10}$$

Combining Equations (7) (8) (9) and (10), we obtain

$$\begin{aligned}
&\|\mathbf{X} - \mathcal{F}_N^{(N)} \circ \mathcal{F}_{N-1}^{(N-1)} \circ \dots \circ \mathcal{F}_1^{(1)}(\mathbf{G})\| \\
&\leq \|\mathcal{I}^{(N)} \circ \mathcal{I}^{(N-1)} \circ \dots \circ \mathcal{I}^{(1)}(\mathbf{X}) - \mathcal{I}^{(N)} \circ \mathcal{F}_{N-1}^{(N-1)} \circ \dots \circ \mathcal{F}_1^{(1)}(\mathbf{G})\| \\
&\quad + \|\mathcal{I}^{(N)} \circ \mathcal{F}_{N-1}^{(N-1)} \circ \dots \circ \mathcal{F}_1^{(1)}(\mathbf{G}) - \mathcal{F}_N^{(N)} \circ \mathcal{F}_{N-1}^{(N-1)} \circ \dots \circ \mathcal{F}_1^{(1)}(\mathbf{G})\| \\
&= \|\mathcal{I}^{(N)}(\mathcal{I}^{(N-1)} \circ \dots \circ \mathcal{I}^{(1)}(\mathbf{X}) - \mathcal{F}_{N-1}^{(N-1)} \circ \dots \circ \mathcal{F}_1^{(1)}(\mathbf{G}))\| + \|(\mathcal{I}^{(N)} - \mathcal{F}_N^{(N)})(\mathcal{F}_{N-1}^{(N-1)} \circ \dots \circ \mathcal{F}_1^{(1)}(\mathbf{G}))\| \\
&\leq \|\mathcal{I}^{(N)}\| \|\mathcal{I}^{(N-1)} \circ \dots \circ \mathcal{I}^{(1)}(\mathbf{X}) - \mathcal{F}_{N-1}^{(N-1)} \circ \dots \circ \mathcal{F}_1^{(1)}(\mathbf{G})\| + \|\mathcal{I}^{(N)} - \mathcal{F}_N^{(N)}\| \|\mathcal{F}_{N-1}^{(N-1)} \circ \dots \circ \mathcal{F}_1^{(1)}(\mathbf{G})\| \\
&\leq \|\mathcal{I}^{(N-1)} \circ \dots \circ \mathcal{I}^{(1)}(\mathbf{X}) - \mathcal{F}_{N-1}^{(N-1)} \circ \dots \circ \mathcal{F}_1^{(1)}(\mathbf{G})\| + \|\mathcal{I}^{(N)} - \mathcal{F}_N^{(N)}\| \|\mathcal{F}_{N-1}^{(N-1)}\| \dots \|\mathcal{F}_1^{(1)}\| \|\mathbf{G}\| \\
&\leq \dots \\
&\leq \|\mathcal{I}^{(1)}(\mathbf{X}) - \mathcal{F}_1^{(1)}(\mathbf{G})\| + \sum_{k=1}^{N-1} \left( \|\mathcal{I}^{(k+1)} - \mathcal{F}_{k+1}^{(k+1)}\| \|\mathbf{G}\| \prod_{j=1}^k \|\mathcal{F}_j^{(j)}\| \right) \\
&\leq \|\mathbf{X} - \mathbf{G}\| + \|\mathcal{I}^{(1)} - \mathcal{F}_1^{(1)}\| \|\mathbf{G}\| + \sum_{k=1}^{N-1} \left( \|\mathcal{I}^{(k+1)} - \mathcal{F}_{k+1}^{(k+1)}\| \|\mathbf{G}\| \prod_{j=1}^k \|\mathcal{F}_j^{(j)}\| \right) \\
&< \frac{\varepsilon}{2} + \frac{\varepsilon}{(2^{N+1} - 2)M} M + \sum_{k=1}^{N-1} \left( \frac{\varepsilon}{(2^{N+1} - 2)M} M \cdot 2^k \right) \\
&= \varepsilon.
\end{aligned}$$

□